Research Square

Preprints are preliminary reports that have not undergone peer review.
They should not be considered conclusive, used to inform clinical practice,
or referenced by the media as validated information.

Silane-Functionalized MgO Nanoflake-Reinforced PLA–Curcumin Nanocomposite Films for Active Grape Packaging

Ramar Dharmaraj
Alagappa University
Arumugam Ayyakannu
arumugama@alagappauniversity.ac.in
Alagappa University

Research Article

Keywords: Magnesium oxide nanoflakes, Silane-functionalized MgO, PLA–curcumin nanocomposite, Active food packaging, Antibacterial films, Shelf-life extension

Posted Date: November 12th, 2026

DOI: https://doi.org/10.21203/rs.3.rs-11205829/v1

License: This work is licensed under a Creative Commons Attribution 4.0 International License.
Read Full License

Additional Declarations: No competing interests reported.

Silane-Functionalized MgO Nanoflake-Reinforced PLA–Curcumin Nanocomposite Films for Active Grape Packaging

Ramar Dharmaraj[a], Arumugam Ayyakannu[a]*

[a] Department of Botany, Alagappa University, Karaikudi 630 003, Tamil Nadu, India

Corresponding author:

* arumugama@alagappauniversity.ac.in (Dr. Arumugam Ayyakannu)

ABSTRACT

Hydrothermally synthesized magnesium oxide (MgO) nanoflakes (NFs) were developed as functional nanofillers for biodegradable active food packaging. X-ray diffraction confirmed a face-centered cubic crystal structure with an average crystallite size of 21.5 nm, while transmission electron microscopy revealed a flake-like morphology with particle sizes of 90–110 nm. The MgO NFs exhibited concentration-dependent antibacterial activity against *Staphylococcus aureus* and *Escherichia coli*, with greater susceptibility observed for *E. coli*. Toxicity assessment using *Artemia salina* nauplii and RAW 264.7 macrophage cells demonstrated excellent biocompatibility without significant cytotoxicity up to 50 μg mL^{-1}. Surface-functionalized MgO, modified with 3-(glycidyloxypropyl)trimethoxysilane, was incorporated into polylactic acid/curcumin (PLA-CRU) films at 1–3% via solvent casting. FTIR, XRD, and SEM analyses confirmed improved interfacial compatibility, enhanced crystallinity, and uniform nanoparticle dispersion within the polymer matrix. The PLA-CRU-3% F-MgO film exhibited complete inhibition of both bacterial strains and the highest antioxidant activity. During grape storage, the nanocomposite films reduced weight loss, maintained pH and

titratable acidity, preserved antioxidant capacity, and effectively delayed fruit deterioration. Overall, the PLA-CRU-3% F-MgO nanocomposite demonstrates strong potential as a biodegradable active packaging material for extending the shelf life and microbiological safety of fresh fruits.

Keywords: Magnesium oxide nanoflakes, Silane-functionalized MgO, PLA–curcumin nanocomposite, Active food packaging, Antibacterial films, Shelf-life extension

1. INTRODUCTION

Nanotechnology has become a key area of materials science due to its wide applications in medicine, energy, and environmental fields [1–3]. Nanoparticles (NPs) exhibit enhanced reactivity and unique optical, electronic, and biological properties because of their high surface-to-volume ratio and tunable physicochemical characteristics [4]. These properties make nanoparticles suitable for advanced technological and biomedical applications [5]. The synthesis method determines the structural and functional properties of nanoparticles [4]. Among various approaches, hydrothermal synthesis produces well-defined nanostructures with controlled morphology under mild conditions [6–8]. Metal oxide nanoparticles, including copper oxide (CuO) [9], zinc oxide (ZnO) [10], titanium dioxide (TiO_2) [11], calcium oxide (CaO), and magnesium oxide (MgO) [7, 8], serve important roles in catalysis, environmental remediation, and biomedical applications.

The MgO nanomaterials (NMs) attract significant attention due to their high surface area, thermal stability, low toxicity, and cost-effectiveness [12]. MgO NPs exhibit antibacterial activity, photocatalytic dye degradation, and cytocompatibility through reactive oxygen species generation and Mg^{2+} ion release [12]. MgO nanoflakes (NFs) provide enhanced surface reactivity and functional performance because of their two-dimensional morphology and high aspect ratio. Recent studies demonstrate the potential of MgO NMs in photocatalytic degradation and

biomedical applications [12]. However, morphology, particle size, and surface characteristics strongly influence their performance. Most studies focus on conventional MgO NPs, while limited research investigates hydrothermally synthesized MgO NFs. Comprehensive studies that simultaneously evaluate structural, photocatalytic, and biological properties remain scarce. In addition, the relationship between nanoflake morphology and multifunctional performance remains unclear, and inconsistent antibacterial and toxicity results require further investigation.

Polylactic acid (PLA) is a prominent bio-based, biodegradable thermoplastic polyester produced by the polymerization of lactic acid derived from the microbial fermentation of renewable biomass feedstocks, including corn starch and sugarcane.[13]. PLA exhibits good mechanical strength and thermal processability, which support its use in packaging, textiles, and 3D printing [14]. However, PLA shows brittleness, weak antibacterial activity, and poor antioxidant properties, which limit its application in food preservation [15]. Researchers improve PLA performance by incorporating NPs and bioactive compounds. Curcumin (CRU), derived from *Curcuma longa*, exhibits antioxidant, anti-inflammatory, and antimicrobial properties. However, poor solubility and bioavailability limit its direct application [16]. Incorporation of CRU into PLA improves crystallinity and enhances food shelf life and safety [17, 18].

The NPs act as effective fillers in biodegradable polymers to enhance antibacterial, barrier, and mechanical properties [18]. However, direct incorporation of metal oxide NPs causes aggregation due to poor interfacial compatibility. Surface functionalization using silane coupling agents improves dispersion, reduces agglomeration, and enhances composite performance, although such strategies remain underexplored. Dowan Kim et al. demonstrated that KH570-functionalized ZnO improved barrier and antibacterial properties in polymer composites [19]. The (3-Glycidyloxypropyl)trimethoxysilane (GPTMS) is a bifunctional silane coupling agent widely used to improve the interfacial adhesion and

dispersion of inorganic nanomaterials in polymer matrices [20]. Heydari et al. reported that GPTMS-mediated covalent functionalization of ZnO nanoparticles with chitosan enhanced biocompatibility toward L929 fibroblast cells at a concentration of 50 μg mL^{-1} [21]. Moreover, GPTMS surface modification has been shown to improve the antibacterial performance of ZnO nanoparticles [22–24].

In this study, MgO nanoflakes were synthesized via a hydrothermal method to obtain materials with enhanced antibacterial, biocompatible, non-toxic, and photocatalytic properties. The synthesized MgO nanoflakes were surface-functionalized and incorporated into a polylactic acid–curcumin (PLA–CRU) matrix. PLA–CRU–MgO composite films were subsequently fabricated using a facile solution-casting technique. The structural, morphological, and functional properties of the composite films were investigated, and their antibacterial efficacy against both Gram-positive and Gram-negative bacterial strains was evaluated. This work aims to develop sustainable bioactive packaging materials with improved antimicrobial performance for potential food-packaging and biomedical applications.

2. MATERIAL AND METHODS

2.1. Chemicals

The magnesium nitrate hexahydrate ($Mg(NO_3)_2 \cdot 6H_2O$) and polyethylene glycol (PEG Mn:200) were procured from Merck (India). The chloroform ($CHCl_3$), ethanol (99.9%), methylene blue ($C_{16}H_{18}ClN_3S$), Sodium hypochlorite (NaOCl) solution, and sodium hydroxide pellets (NaOH) were obtained from SRL (India). (3-Glycidyloxypropyl)-trimethoxysilane (GMT) was sourced from Sigma-Aldrich (USA). Ciprofloxacin (CIP; 5 mg), and Phenolphthalein indicator were obtained from HiMedia Laboratories Pvt. Ltd., Mumbai, India. Polylactic acid

(PLA) pellets (grade 4043D) were procured from Natur-Tec India Pvt. Ltd., India. Fresh table grapes (*Vitis vinifera* L.) used for the packaging study were purchased from a local commercial market in Karaikudi, Tamil Nadu, India. Deionized (DI) water was used throughout all experiments.

2.2. Hydrothermal Synthesis of Magnesium Oxide Nanoflakes (MgO NFs)

The magnesium oxide nanoflakes (MgO NFs) were synthesized via the hydrothermal method. A 0.1 mM of magnesium nitrate was prepared with 400 mL of DI water and stirred for 30 min. Then, 20 g of PEG was slowly added to the magnesium nitrate solution and stirred continuously for 30 min. Subsequently, 400 mL of 0.1 mM NaOH was added dropwise into the magnesium nitrate solution under constant stirring at room temperature (37 °C) for 1 h. The resulting mixture was transferred to a 1 L Teflon-lined autoclave sealed with a stainless-steel screw-type lid. The autoclave was heated at 180 °C for 12 h in a hot air oven. After cooling, the sample was collected and centrifuged at 5000 rpm. The precipitate was washed several times with DI water, followed by ethanol. The collected precipitate was dried at 60 °C overnight in a hot air oven and subsequently calcined at 400 °C for 4 h (Scheme 1A).

2.3. Functionalization of MgO NFs (F-MgO)

The 1 g of MgO NFs was dispersed in 1000 mL of DI water and stirred at 37 °C for 1 h. Subsequently, 1 g of GMT silane coupling agent (used as a compatibilizer) was added, and the mixture was stirred for an additional 24 h. Then, the product was centrifuged at 5000 rpm Further, received samples was washed three times with DI water and dried at 60 °C. The obtained functionalized MgO (F-MgO) was stored in a desiccator (Scheme 1B).

2.4. Fabrication of PLA, PLA-CRU, and PLA-CRU-F-MgO nanocomposite films via the solvent casting method

Initially, 4 g of PLA was gradually dissolved in 100 mL of $CHCl_3$ under continuous stirring for 1 h, followed by further stirring at 37 °C for 5 h until complete dissolution (Scheme 1C). For PLA–CRU films, 2% CRU (relative to PLA weight) was first dissolved in 100 mL of $CHCl_3$ for 1 h (Scheme 1D), after which 4 g of PLA was added and stirred vigorously for 1 h, followed by an additional 5 h of stirring at 37 °C. For the preparation of PLA–CRU–F-MgO nanocomposite films, varying contents of F-MgO (1, 2, and 3% relative to PLA weight) were incorporated into the CRU solution (Scheme 1E). Each mixture was sonicated for 2 min to ensure uniform dispersion. Subsequently, 4 g of PLA was added to the CRU–F-MgO mixture and stirred vigorously for 1 h, followed by stirring at 37 °C for 5 h. Finally, 16 g of the resulting solution was cast into a glass Petri dish (90 mm × 15 mm) and dried at 37 °C for 72 h. The obtained films were peeled off and conditioned at 25 °C and 50% relative humidity (RH) for 72 h.

2.5. Characterization

The phase purity and crystalline size of MgO nanoflakes (NFs) were analyzed using X-ray diffraction (XRD) in the 2θ range of 10° to 80° using a diffractometer system (XPERT-PRO, PANalytical). Optical analysis was performed between 200–800 nm with a JASCO V-750 UV-Vis spectrometer (Jasco 9 International Co., Ltd., Tokyo, Japan) Fourier transform infrared spectroscopy (FT-IR) analysis was conducted in the range of 4500-500 cm^{-1} using a BRUKER (ALPHA II) instrument. The morphology and topography of MgO NFs and nanocomposite films were characterized by scanning electron microscopy (SEM) (TESCAN VEGA3 XMU), while elemental composition was examined using energy-dispersive X-ray spectroscopy (EDX). The morphology and particle size of the MgO NFs were analyzed using high-resolution transmission

electron microscopy (HR-TEM) with a Tecnai G2 20 S-TWIN TEM at 200 kV. X-ray photoelectron spectroscopy (XPS) was performed with a VERSAPROBE III instrument, using a monochromatic Al Kα X-ray source with a 15 μm beam size.

2.6. Antioxidant activity

2.6.1. DPPH activity

For testing the radical scavenging effect, the DPPH test was performed by wrapping the film (40 mg thick, 2 cm x 2 cm) tightly in 5 mL of ethanol and then shaking for 30 min at 25 °C (the film was kept completely submerged). The mixture was then centrifuged at 6000 rpm for 10 min to obtain the supernatant. 1 mL of the supernatant was then added to 3 mL of 0.2 mM DPPH in ethanol and incubated for 30 min in the dark. After 30 min, the absorbance of each sample was measured at 517 nm using a UV-visible spectrophotometer. To calculate the amount of DPPH cleared, 1 mL of 0.2 mM DPPH in ethanol and 3 mL of ethanol were mixed for 30 minutes in the dark and their absorbance was measured at 517 nm, and finally 1 mL of supernatant was added to 3 mL of ethanol and incubated for 30 minutes in the dark and their absorbance was measured at 517 nm, then using the equation (Eq.1.) to determine the amount of DPPH radical clearance.

$$\mathrm{DPPH}\ (\%) = (\mathrm{A1} - \mathrm{A2})/\mathrm{A3} \times 100 \qquad \text{--------- (1)}$$

where A1 is the absorbance of the film and DPPH, A2 is the absorbance of the film and ethanol, and A3 is the absorbance of DPPH and ethanol [25].

2.6.2. ABTS activity

For the ABTS radical scavenging assay, ABTS solution (7.4 mmol L^{-1}) was mixed with potassium persulfate (2.6 mmol L^{-1}) in a 1:1 (v/v) ratio and incubated in the dark for 12 h. The resulting solution was diluted with ethanol to obtain an absorbance of 0.70 ± 0.02 at 734 nm. Subsequently, 100 µL of the sample was mixed with 1 mL of the diluted ABTS solution and incubated in the dark for 6 min. The absorbance was then recorded at 734 nm using a UV–Vis spectrophotometer

(A_1). Ethanol (100 µL) was used as the control

(A_0). The ABTS radical scavenging activity was calculated using Eq. (2).

$$\text{ABTS}\ (\%) = (\text{A0} - \text{A1})/\text{A0} \times 100 \qquad \text{--------- (2)}$$

where A1 was the absorbance of ABTS of the test film, and A0 was the absorbance of ABTS of the blank film [25].

2.76. Antibacterial activity

2.7.1. Antibacterial activity of MgO NFs

The antibacterial effect of MgO NFs was assessed using the agar disk diffusion method against *Staphylococcus aureus* and *Escherichia coli*. Bacterial cultures were grown in nutrient broth (37 °C, 24 h), spread on nutrient agar plates, and 6 mm disk were filled with MgO NF solutions (NC, 300, and 500 µg). Ciprofloxacin (5 mg) served as the positive control. After incubation (37 °C, 24 h), inhibition zones were measured. All tests were conducted in triplicate, and mean values were reported.

2.7.2. Antibacterial activity of nanocomposite films

Antibacterial tests on PLA, PLA-CRU, PLA-CRU-1%-F-MgO, PLA-CRU-2%-F-MgO, and PLA-CRU-3%-F-MgO nanocomposite films were conducted following the JIS Z 2801 standard with a slight modification. *S. aureus* and *E. coli* were cultured on tryptic soy and MacConkey agar (38 °C, 24 h), and a single colony was transferred to nutrient broth. Sterilized all composite films (5 cm × 5 cm) were inoculated with 0.4 mL bacterial suspension, covered with sterile polyethylene film, and incubated (37 °C, 24 h). After washing with saline, serial dilutions of the bacterial suspensions were plated via the drop method onto agar plates and incubated (37 °C, 48 h) to assess antibacterial activity [26]. The antibacterial activity (R) was determined by calculating the bacterial colony-forming units (CFUs) using the following equation (Eq. 3):

$$R\,(\%) = (B - C)/B \times 100 \quad \text{--------- (3)}$$

where B is the CFU in the control group, and C is the CFU in the treated group after 24 h. All experiments were conducted in triplicate to ensure reproducibility.

2.8. Cell culture and cell viability assay

RAW 264.7 macrophage cells were cultured in Dulbecco's Modified Eagle's Medium (DMEM) supplemented with 10% fetal bovine serum (FBS) at 37 °C in a humidified incubator containing 5% CO_2. The cells were seeded into 96-well plates at a density of 5×10^4 cells mL^{-1} and incubated for 24 h. The culture medium was then replaced with fresh medium containing either the control or MgO nanoflakes (MgO NFs) at concentrations of 0.1, 0.5, 1, 5, 10, 25, and 50 μg mL^{-1}, followed by incubation for an additional 24 h. Cell viability was determined using the EZCytox assay kit (DoGenBio, Republic of Korea), and the absorbance was measured at 450 and 600 nm using a microplate reader (Epoch 2, BioTek, USA).

2.9. In vitro toxicity activity of MgO NFs tested against A. salina nauplii

One gram of *Artemia salina* cysts was added to 1000 mL of sterilized seawater (29 ppt) at 30 °C, with aeration under 1500 LUX light intensity. After 24 h, healthy nauplii were collected for experimental studies. A 12-well plate was prepared, each well containing 2 mL of seawater and then (n = 20) *A. salina* nauplii. MgO NFs were dispersed in seawater using ultrasonic vibration (100 W, 30 kHz) for 30 min. Different concentrations of MgO NFs (0.25, 0.50, 0.75, and 1.00 μg/mL) were added to the wells. The setup was aerated to maintain the volume, and the plate was incubated at room temperature. Nauplii mobility and lethargy were observed, with mortality recorded at 12 and 24 h intervals. The mortality rate for MgO NFs was calculated and compared to the control using the percentage mortality formula (Eq. 4).

$$\% \text{ Mortality} = \text{Number of dead organisms} / \text{The initial number of live organisms} \times 100$$

---------- (4)

2.10 Application of film for grape preservation

Fresh table grapes (*Vitis vinifera* L.) were procured from a local commercial market and transported to the laboratory within 2 h. Damaged, infected, cracked, shriveled, or defective grapes were discarded. The selected grapes were washed with distilled water, surface-sanitized by immersion in 0.1% (v/v) sodium hypochlorite solution for 2 min, rinsed three times with sterile distilled water, and air-dried under aseptic conditions. Uniform grapes (15 g per package) were randomly assigned to five treatment groups: PLA, PLA–CRU, PLA–CRU–1% F-MgO, PLA–CRU–2% F-MgO, and PLA–CRU–3% F-MgO. Each package was heat-sealed with the corresponding biodegradable film at 120–130 °C for 3–5 s. The packaged grapes were stored in a Biological Oxygen Demand (BOD) incubator (Model 560 BOD, Biolab Scientific Ltd., Markham, ON, Canada) at 25 ± 2 °C and 50 ± 5% relative humidity for 15 days. Samples were analyzed at 0, 3, 6, 9, 12, and 15 days for weight loss, pH, titratable acidity, and DPPH radical scavenging activity. Changes in the external appearance of the grapes were recorded photographically throughout the storage period.[27, 28].

2.10.1. Visual Appearance Evaluation

The visual quality of grapes packaged with PLA, PLA–CRU, PLA–CRU–1% F-MgO, PLA–CRU–2% F-MgO, and PLA–CRU–3% F-MgO films was monitored during storage. Representative photographs were taken at 0, 3, 6, 9, 12, and 15 days under identical lighting conditions to assess changes in color, shriveling, fungal decay, and overall appearance.

2.10.2. Weight loss

The weight of each packaged grape sample was measured at 0, 3, 6, 9, 12, and 15 days using a digital analytical balance (±0.001 g). The percentage weight loss was calculated using Eq. (5):

$$Weight\ loss\ (\%) = W0 - Wt/W0 \times 100 \quad \text{---------- (5)}$$

where W_0 is the initial weight (g) and W_t is the weight of the grapes (g) at each storage interval.

2.10.3. pH Measurement

Approximately 10 g of grape berries were homogenized with 90 mL of distilled water, and the homogenate was filtered through Whatman No. 1 filter paper. The pH of the filtrate was measured using a calibrated digital pH meter at room temperature.

2.10.4. Titratable Acidity

Titratable acidity (TA) was determined following the [27, 29] standard titration procedure. Briefly, 10 mL of grape juice was diluted with distilled water and titrated against 0.1 N sodium hydroxide (NaOH) using phenolphthalein as the endpoint indicator. Results were expressed as percentage citric acid equivalent and calculated according to (Eq.6)

$$TA\ (\%) = V \times N \times EW \times 100/Vs \times 1000 \quad \text{---------- (6)}$$

where: V = Volume of NaOH (mL), N = Normality of NaOH, EW = Equivalent weight of citric acid (75.04), Vs = Sample volume (10 mL).

2.10.5. DPPH Free Radical Scavenging Activity

The antioxidant activity of grape extracts was determined using the DPPH radical scavenging assay according to Brand-Williams et al. (1995) with slight modifications. Briefly, 1 mL of grape extract was mixed with 3 mL of 0.1 mM DPPH methanolic solution and incubated in the dark for 30 min at room temperature. The absorbance was measured at 517 nm using a UV–Visible spectrophotometer.

The percentage of DPPH radical scavenging activity was calculated as follows (Eq.7)

$$\text{DPPH scavenging activity } (\%) = Ac - As/Ac \times 100 \text{ ---------- (7)}$$

where: Ac = Absorbance of control, As = Absorbance of sample

2.11. Statistical significance

The experimental data were reported as the mean and standard deviations (SD). For statistical evaluation, a paired t-test was performed using SPSS Statistics software and Origin Lab 2024 software. The significance was denoted using p-values as follows: $p < 0.05$ ($*$), $p < 0.01$ ($**$), and $p < 0.001$ ($***$).

3. RESULTS AND DISCUSSIONS

3.1. UV-Vis-DRS analysis of MgO NFs

The synthesized MgO NFs were characterized using UV-Vis-DRS, as illustrated in (Figure 1) The absorption spectrum exhibited a pronounced peak at 285 nm, indicating the optical properties of the MgO NFs. The optical direct band gap was calculated using the Tauc plot equation (Eq. 8):

$$(\alpha h\nu)^2 = A(h\nu - Eg) \quad \text{- - (Eq. 8)}$$

where ***α*** represents the optical absorption coefficient, ***hν*** is the photon energy, **Eg** is the direct energy gap, and **A** is a proportionality constant. The band gap energy of the synthesized MgO NFs was determined to be 4.2 eV using Tauc plot analysis. Sagadevan et al. reported the successful synthesis of MgO nanoballs via the hydrothermal method, which exhibited an absorption peak at 280 nm and a band gap energy of 5.14 eV [30].

The MgO NFs showed an absorption peak at 286 nm, higher than the 163 nm seen in bulk MgO due to excitonic transitions in single crystals. This shift is attributed to surface oxide ion (O^{2-}) coordination, with reduced ion coordination lowering the electrostatic potential and energy required for the process [31, 32].

3.2. FTIR analysis of MgO NFs

3.2.1. FTIR analysis of MgO NFs

The FTIR spectrum of MgO NFs is presented. A broad absorption band at 3345 cm^{-1} is attributed to O–H stretching vibrations from adsorbed water and surface hydroxyl groups (Mg–OH) [33]. As shown in (Figure 2A), the peak at 2925 cm^{-1} corresponds to C–H stretching vibrations of residual organic species from PEG [34]. The band at 1637 cm^{-1} is assigned to H–O–H bending of physically adsorbed water. Peaks at 1440 cm^{-1} and 1375 cm^{-1} are associated with carbonate (CO_3^{2-}) species [35]. The absorptions at 885 cm^{-1} are attributed to C–O stretching [36]. Importantly, the strong band at 543 cm^{-1} corresponds to Mg–O stretching vibrations, confirming the formation of the MgO crystalline lattice [37]. These peaks are in good agreement with previously reported work [34]. As illustrated in the (Figure 2B) the FTIR spectrum of GMT exhibits characteristic absorption bands at 2935 and 2875 cm^{-1} corresponding to C–H stretching vibrations, 1733 cm^{-1} attributed to C=O stretching, and 1444 cm^{-1} assigned to CH_2 bending vibrations. The band at 1195 cm^{-1} is associated with Si–CH_3 symmetric stretching, while the peak at 1015 cm^{-1} corresponds to Si–O–C stretching. Additionally, the absorption at 906 cm^{-1} is attributed to epoxide ring deformation, and the band at 795 cm^{-1} corresponds to Si–C stretching vibrations [38, 39]. (Figure 2C) presents the FTIR spectrum of GMT-functionalized MgO F-MgO, confirming

successful surface modification through the appearance of silane-related bands along with the characteristic Mg–O vibration. The broad band at 3308 cm^{-1} corresponds to O–H stretching of surface hydroxyl groups and adsorbed moisture, while the peak at 1595 cm^{-1} is attributed to H–O–H bending. The absorptions at 1430 and 1315 cm^{-1} are associated with carbonate and C–H deformation vibrations. Notably, the bands at 1160 and 1030 cm^{-1} indicate Si–O–C and Si–O–Si/Si–O–Mg stretching, confirming GMT grafting onto the MgO surface. The strong band at 555 cm^{-1} corresponds to Mg–O stretching, verifying that the MgO lattice remained intact after functionalization.

3.2.2. Composite films appearance and functional analysis

The appearance of the prepared nanocomposite films. The PLA film exhibits high transparency. (Figure 2D) The incorporation of 2% CRU imparts a yellowish color to the film. The addition of 1–3% F-MgO increases the whiteness of the PLA–2%CRU composite films. The increase in F-MgO content reduces film transparency and enhances opacity. The dispersed F-MgO scatter light within the polymer matrix and alter the optical properties of the composite films.

As depicted in (Figure 2D), the FTIR spectrum of the PLA film exhibits characteristic absorption peaks at 2920, 2848, 1745, 1445, 1356, 1264, 1180, 1075, 1036, 952, 868, and 750 cm^{-1}[26]. The bands at 2920 and 2848 cm^{-1} correspond to C–H stretching vibrations. The sharp peak at 1745 cm^{-1} is attributed to the C=O stretching vibration of the ester functional group. The peaks at 1445 and 1356 cm^{-1} represent asymmetric and symmetric C–H deformation vibrations, respectively. The C–O stretching vibrations appear in the regions of 1264–1180 cm^{-1} and at 1075 cm^{-1}. The peak at 1036 cm^{-1} is assigned to C–CH_3 stretching, while the band at 952 cm^{-1} corresponds to C–C backbone stretching. The absorptions at 868 and 750 cm^{-1} are associated with C–C stretching and CH rocking vibrations, respectively [26, 40]. (Figure 2D), the PLA–2% CRU film

exhibits similar characteristic peaks to those of pure PLA. However, with increasing F-MgO content, the intensity of the C=O, C–H, and C–O bands increases (Figure 2D). This enhancement suggests improved PLA nucleation and stronger interfacial interactions induced by the incorporation of F-MgO. The PLA–2%CRU film exhibits characteristic absorption bands similar to those of pure PLA. However, with increasing F-MgO content (1–3%), the intensity of the peaks at 1745, 1264, 1180, and 1075 cm^{-1}, corresponding to C=O and C–O stretching vibrations, increases. The film containing 2% F-MgO shows improved interfacial interaction with the PLA–CRU matrix. In contrast, lower (1%) and higher (3%) F-MgO loadings result in poorer dispersion and increased particle aggregation within the composite matrix.

3.3. XRD analysis of MgO NFs and Composite films, and Visual appearance of PLA, PLA-CRU, PLA-CRU-F-MgO films

The XRD analysis of MgO NFs is presented in (Figure 3A). The synthesized MgO NFs exhibited well-defined diffraction peaks at 2θ values of 37.89°, 42.74°, 50.65°, 58.62°, 62.06°, and 78.49°, corresponding to the (111), (200), (220), (311), and (222) planes, respectively. These peaks are characteristic of the face-centered cubic (FCC) structure of MgO and are well-matched with the Joint Committee on Powder Diffraction Standards (JCPDS) card no. 78-0430. The average crystallite size (D) of the MgO NFs was evaluated using the Scherrer formula (Eq. 9).

$$D = K\lambda/\beta cos\theta \quad \text{- - - (Eq. 9)}$$

where K is the shape factor (with a typical value of 0.9), λ represents the wavelength of X-ray radiation (0.154 nm), β is the full width at half maximum (FWHM) of the diffraction peak, and θ denotes the Bragg angle. The calculated average crystallite size of the MgO NFs was 20.49 nm. The MgO sample exhibited a nanoflake structure that developed through specific mechanisms. The PEG was used as a surfactant during the synthesis process. PEG acts as a proton acceptor, facilitating growth along the (220) and (311) directions. These directions are associated with

higher energy surfaces, which emerge under specific hydrothermal conditions. This suggests a controlled and stable growth of MgO NFs in these orientations, contributing to their crystallinity. Balamurugan et al. reported the synthesis of nanocrystalline MgO particles via a combustion method followed by annealing and studied their crystal structure. The results confirmed that the synthesized MgO NPs were polycrystalline and exhibited a cubic crystal structure [41]. Abbas and Adim reported the synthesis of crystalline MgO NPs using an atmospheric non-thermal plasma jet, achieving particle sizes of 9.36 ± 1.42 nm (10 min) and 14.25 ± 2.36 nm (12 min). XRD patterns showed characteristic peaks corresponding to cubic MgO NPs [42]. (Figure 3B) illustrates the XRD pattern of the pure PLA film, which exhibits a broad diffraction band between 12° and 22.5°, confirming its amorphous structure. The solution casting method inhibits the orderly arrangement of polymer chains and prevents the development of crystallinity [43, 44]. In contrast, the PLA–2%CRU film displays characteristic diffraction peaks at 12.1°, 14.6°, 16.5°, 18.9°, and 22.1°, corresponding to the (103), (100), (110)/(200), (203), and (015) planes of the α-form crystalline PLA [26]. The CRU acts as a nucleating agent and enhances PLA crystallinity by promoting chain alignment and crystalline growth while reducing the amorphous phase [18]. The incorporation of 1–3% F-MgO into the PLA–CRU film increases the intensity of the characteristic PLA diffraction peaks, indicating enhanced crystallinity. The composite films exhibit additional peaks at 37.84°, 42.29°, and 50.35°, which correspond to the (200), (220), and (311) planes of MgO. These peaks confirm the presence of MgO and further support the improvement in crystallinity. The well-dispersed F-MgO acts as an effective nucleating agent and promotes PLA crystallization. The film containing 3% F-MgO exhibits the most intense and well-defined peaks. The improved intermolecular interactions between PLA chains increase structural regularity and overall crystallinity. These findings are consistent with previous studies [18, 26].

On the other hand, the crystallinity index (CrI) of the fabricated films was determined using the empirical equation (Eq. 10).

$$\text{Crystallinity Index (\%)} = [(I_{Cr}/(I_{Cr} + I_{non-Cr})] \times 100 \quad \text{--------- (10)}$$

Where I_{Cr} is the integrated intensity of the crystalline phases and I_{non-Cr} is the integrated intensity of the non-crystalline (amorphous) background phase.

Shown (Figure 3C). The pure PLA film exhibits a low crystallinity index (CrI) of 4.71%, which is typical of amorphous polymers, as confirmed by the broad and low-intensity XRD peak (Figure 3C). The PLA–2%–CRU composite film shows an increased CrI of 26.71%, indicating that CRU enhances polymer crystallization. Roy and Rhim (2020) reported that the addition of 1.5 wt% CRU increased the CrI of PLA to 29.9%, demonstrating its role as a nucleating agent [18]. The incorporation of 1% F-MgO further increases the CrI to 34.35%, suggesting that MgO promotes crystallization within the PLA–2%CRU matrix, as supported by the appearance of distinct MgO diffraction peaks. However, the film containing 2% F-MgO exhibits a reduced CrI of 28.97%, indicating that higher MgO loading interferes with polymer chain organization. The film with 3% F-MgO shows a further decrease in CrI to 27.21%, suggesting that excessive F-MgO disrupts crystallization, possibly due to particle agglomeration.

As shown in (Figure S1), the digital photographs of neat PLA, PLA–CRU, and PLA–CRU– F–MgO nanocomposite films containing different loadings (1–3 wt.%) of silane-functionalized MgO nanoflakes. Neat PLA exhibited a transparent and colorless appearance with high optical clarity. Incorporation of curcumin into the PLA matrix produced a bright yellow film, confirming the homogeneous dispersion of the natural pigment throughout the polymer matrix. Upon addition of functionalized MgO NFs, the film color gradually changed from yellow to

orange with increasing F-MgO content. The PLA–CRU–1%F–MgO film retained good transparency, whereas the 2 wt.% and 3 wt.% F-MgO films became progressively darker and slightly opaquer. This color variation can be attributed to enhanced light scattering by the dispersed MgO NFs and their interaction with curcumin and the PLA matrix. Despite the increased filler loading, all films remained continuous, flexible, and free from visible cracks or phase separation, indicating good compatibility between the silane-functionalized MgO nanoflakes and the PLA–CRU matrix. The uniform visual appearance further suggests effective dispersion of the functionalized nanofillers, consistent with the FTIR, XRD, and SEM results. These observations demonstrate that surface functionalization of MgO improves filler–matrix interfacial adhesion while maintaining the structural integrity of the biodegradable nanocomposite films.

3.4. SEM, elemental mapping, EDX, TEM and SAED analysis of MgO NFs

The presents SEM micrographs of MgO NFs, (Figure 4 A-C) showing predominantly flake-like structures in an agglomerated form. This indicates that the MgO nanoflakes tend to cluster together, forming larger aggregates while maintaining their characteristic thin, plate-like morphology. The elemental mapping images (Figure 4D-F) display green and brown colors corresponding to oxygen (O) and magnesium (Mg), and silica (Si) with compositions of weight percentage at 36.07 49.32 % 63.93, 49.64 %, and 1.04%, respectively. The EDX spectrum (Figure 4G) exhibits characteristic peaks at 0.5 and 1.3 keV, confirming the presence of O and Mg elements. The atomic and weight percentages of O and Mg are displayed in (Figure 4G). No additional elemental peaks were detected in the EDX analysis, confirming the successful synthesis of pure MgO NFs without detectable impurities. The TEM images revealed that the synthesized MgO NFs exhibited distinct flake-like morphologies, showing the characteristic of MgO nanostructures (Figure 5 A, C), thereby confirming successful synthesis. The particle size ranged from 28.62

to 124.69 nm, with an average size of 80.20 nm (Figure 5E). These observations are consistent with the SEM analysis while providing higher-resolution structural details. (Figure 5D) The SAED patterns displayed well-defined diffraction rings, indicating the crystalline nature of the MgO NFs [45]. The observed diffraction rings correspond to the (200), (220), and (311) lattice planes, in agreement with the XRD results, thus confirming the FCC crystal structure of MgO.

3.5. Morphological, elemental mapping, EDX analysis of composite films

The SEM images illustrate the morphological changes in the fabricated films (Figure 6A- E). The neat PLA film exhibits a smooth and homogeneous surface. The incorporation of CRU introduces surface irregularities, indicating its successful integration into the PLA matrix. The PLA–2%CRU–1%F-MgO film shows well-dispersed F-MgO nanoflakes with minimal aggregation, suggesting effective interfacial interaction and uniform distribution. In contrast, the films containing 2% and 3% F-MgO exhibit noticeable particle agglomeration, which reduces surface homogeneity and weakens interfacial adhesion [18]. The addition of F-MgO significantly modifies the film morphology, and the 1% F-MgO concentration provides the most balanced dispersion and structural integrity. The elemental mapping images (Figure S2) demonstrate uniform carbon distribution, representing the continuous PLA and CRU polymer chains. The oxygen signal appears throughout the matrix and corresponds to PLA, CRU, and F-MgO components. The magnesium signal distributes evenly across the film surface, confirming the successful incorporation of F-MgO within the PLA–CRU matrix. Overall, the mapping results confirm uniform nanoparticle dispersion and preservation of matrix integrity. The EDX analysis (Figure S3) shows that pure PLA and PLA–CRU films consist mainly of carbon (44.71 and 44.62 wt.%) and oxygen (55.29 and 55.39 wt.%). The incorporation of F-MgO increases the magnesium content from 1% to 3% while slightly reducing carbon and oxygen percentages. The atomic percentage results follow a similar trend. These findings indicate that 1% F-MgO achieves uniform dispersion and strong

interfacial interaction, whereas higher loadings promote aggregation, consistent with the SEM observations (Table 1). The EDX results confirm the successful incorporation of F-MgO into the PLA, PLA–CRU, and PLA-CRU-F-MgO nanocomposite films.

3.6. XPS Analysis of MgO Nanoflakes

The XPS analysis confirmed the elemental composition and chemical states of MgO NFs (Figure 7A). Survey spectrum. The C 1s spectrum exhibited deconvoluted peaks at 284.68, 286.01, 288.37, and 289.60 eV, corresponding to C–C/C–H, C–O, O–C=O, [46, 47], and carbonate species, respectively, indicating the presence of adventitious carbon and residual PEG-derived functional groups (Figure 7 B). The O 1s spectrum showed peaks at 529.04, 530.14, 530.88, 531.78, and 533.26 eV, which were assigned to lattice oxygen (O^{2-}), oxygen vacancies (V_o), surface hydroxyl (–OH) groups, chemisorbed oxygen (Oβ), and adsorbed water molecules, [48–50].These oxygen species confirm the presence of surface defects and active sites, which are beneficial for catalytic and biological performance (Figure 7C). The Mg core-level spectra further verified the chemical state of magnesium.

The Mg 1s peak at 1303.95 eV confirmed Mg^{2+}–O in the MgO lattice, while the higher binding energy peak at 1306.92 eV indicated surface hydroxylated Mg–OH species [51], (Figure7D).

Similarly, the Mg 2s spectrum displayed peaks at 88.37, 90.55, 92.05, and 93.22 eV [52] (Figure 7E), and the Mg 2p spectrum showed peaks at 49.50, 50.99, 52.79, and 54.50 eV, corresponding to lattice Mg^{2+}, surface Mg–OH, and defect-related or adsorbed Mg species [53, 54] (Figure 7F). The high fitting accuracy ($R^2 > 0.98$) confirms the reliability of the deconvolution. Overall, the XPS results demonstrate that Mg exists predominantly in the Mg^{2+} oxidation state, while oxygen vacancies, hydroxyl groups, and adsorbed species contribute to surface heterogeneity. These features enhance adsorption behavior, photocatalytic activity, and biological interactions of MgO NFs.

3.7. Antioxidant Activity of composite films

The antioxidant activity of all the composite films was assessed using the ABTS•+ and DPPH• assays, as shown in (Figure 8A, B). The PLA film exhibited low antioxidant activity, with ABTS and DPPH radical scavenging efficiencies of 6.04% and 22.06%, respectively. Incorporation of curcumin (CRU) markedly improved the antioxidant performance, increasing the ABTS and DPPH scavenging activities to 44.37% and 39.05%, respectively. Furthermore, the addition of 1–3 wt.% functionalized MgO nanoflakes (F-MgO) to the PLA–CRU films further enhanced the radical scavenging activity, with ABTS values increasing to 44.03–79.90% and DPPH values to 39.90–62.59%. This enhanced antioxidant activity is primarily attributed to the phenolic hydroxyl groups and conjugated molecular structure of curcumin, which effectively neutralize $ABTS^{\bullet+}$ and DPPH• radicals through hydrogen atom transfer and single-electron transfer mechanisms [18]. These findings are consistent with previous reports demonstrating that the incorporation of curcumin significantly improves the antioxidant properties of PLA-based films. For example, Roy and Rhim reported that the DPPH and ABTS radical-scavenging activities increased from 1.8% and 3.1% for neat PLA films to 76.6% and 94.7%, respectively, after incorporating 1.5 wt.% curcumin [18]. Similarly, earlier studies showed that the addition of curcumin enhanced the DPPH radical scavenging activity of PLA films from 16.8% to 83%, confirming the strong free radical scavenging ability of curcumin through hydrogen donation from its phenolic groups [55]. Dai et al. (2022) reported that PLA films exhibited negligible antioxidant activity (8% DPPH), and the incorporation of 3 wt% ZnO NPs showed only a slight increase (8.7%). Similarly, ABTS results confirmed minimal activity for both PLA and PLA/ZnO films, indicating that ZnO alone does not significantly enhance antioxidant performance. However, the addition of pomegranate peel extract (0.5-2 wt.%) in the PLA/ZnO films markedly improved antioxidant activity due to the presence of flavonoids,

phenolics, and proanthocyanidins [25, 56]. The addition of F-MgO enhances antioxidant performance through synergistic surface-mediated electron transfer within the polymer matrix, thereby promoting sustained antioxidant activity.

3.8. Antibacterial Activity

The antibacterial activity of MgO NFs was evaluated using the disk diffusion method at various concentrations the disk size (6 mm).As expected, the positive control (ciprofloxacin disk) exhibited superior antibacterial activity, with zones of inhibition (ZOI) of 18 mm and 14 mm against *S. aureus* and *E. coli*, respectively, as shown in (Figure 9A-C). In contrast, MgO NF disks containing NC (Negative Control), 3, and 5 mg were tested against both bacterial strains. For *S. aureus*, the observed ZOI values were 0, 11.66, and 15.66 mm, respectively, while for *E. coli*, the ZOI values were 0, 7.66, and 12 mm, respectively. These results indicate a concentration-dependent antibacterial effect of MgO NFs. The slightly higher susceptibility of *S. aureus* (Gram-positive) compared to *E. coli* (Gram-negative) due to attributed to differences in their cell wall structures. Gram-negative bacteria possess an outer lipopolysaccharide membrane that acts as an additional barrier, reducing NFs penetration. In contrast, Gram-positive bacteria have a thicker, multi-layered peptidoglycan cell wall, making them more vulnerable to NFs-induced membrane disruption. The antibacterial mechanism of MgO NFs is likely associated with reactive oxygen species (ROS) generation, Mg^{2+} ion release, and direct interaction with the bacterial cell membrane, leading to structural damage and cell death. Akshaykranth et al. (2021) reported that green- and chemically synthesized MgO NPs were calcined at 200 °C (4 h) and 400 °C (4 h), respectively. The samples were evaluated for antibacterial activity against *Bacillus subtilis*, *S. aureus*, *E. coli*, and *Proteus vulgaris* at 2 mg/mL (20-80 µL loading) using the disk diffusion method. Both samples exhibited dose-dependent antibacterial activity; however, the green-synthesized MgO NPs showed superior performance compared to

the chemically synthesized MgO NPs. This enhanced activity is attributed to differences in particle size, shape, concentration, calcination conditions, and the presence of surface organic biomolecules [57]. Rajiv Periakaruppan et al. (2023) reported that green-synthesized MgO nanoparticles exhibited dose-dependent antibacterial activity against *Streptococcus* sp., with a ZOI of 14.5 ± 0.4 mm at 75 /mL, which is comparable to the ZOI of 14.5 ± 0.2 mm observed for tetracycline (10 µg/mL) [58]. Thamizharasan et al. (2024) reported that green-synthesized MgO NPs (1 mg/mL, 50 µL loading) were tested against *Porphyromonas gingivalis*, *S. salivarius*, *S. mutans*, and *S. mitis* using the agar well diffusion method. The ZOI were 18, 14, 12.5, and 11 mm, respectively. *P. gingivalis* showed the highest susceptibility, attributed to its thinner peptidoglycan layer and ROS generation from surface defects and oxygen vacancies in MgO NPs [59]. The present investigation reviled that the antibacterial activity result showed that the synthesis of MgO NFs showed better activity in both bacterial strains, with *S. aureus* being more effectively inhibited.

3.9. Cytotoxicity activity of Mg NFs

The cytotoxicity of MgO NFs toward RAW 264.7 macrophages was evaluated after 24 h exposure (0.1–50 µg/mL). As shown (Figure 10A, B), no cytotoxic effects were observed across the tested concentrations. Cell viability increased slightly at lower doses, reaching at 128.51% at 0.5 µg/mL and 134.32% at 5 µg/mL ($p < 0.05$), suggesting enhanced metabolic activity. Even at higher concentrations (10–50 µg/mL), viability remained 124.76%, with 50 µg/mL maintaining 112.25%. The increased viability may be attributed to mild cellular stimulation rather than toxicity. Overall, MgO NFs exhibited excellent cytocompatibility up to 50 µg/mL, supporting their potential for biomedical and active packaging applications. Kasi et al. (2025) reported that MgO NFs synthesized at 400, 500, and 600 °C were biocompatible at low concentrations (0.1–20

µg/mL), while MgO-400 °C showed slight cytotoxicity at higher concentrations (100–200 µg/mL). The cytotoxicity depended on particle size, surface area, and concentration, as smaller MgO-400 °C particles released more Mg^{2+} ions and generated higher ROS levels. At low doses, Mg^{2+} promoted cell growth, whereas excessive ion release at high doses induced oxidative stress. In contrast, larger MgO-500 °C and MgO-600 °C particles exhibited lower ion release and ROS production, resulting in improved biocompatibility [12]. Ge et al. (2011) reported that 100 nm MgO NPs were non-toxic at 200 µg/mL. By contrast, it showed toxicity above 500 µg/mL on human umbilical vein endothelial cells [60]. Mittag et al. (2019) observed no cytotoxic or genotoxic effects of 50–70 nm MgO (0.001–100 µg/mL) in intestinal HT29 cells [61]. Similarly, Patel et al. reported no significant cytotoxicity of 30 nm MgO up to 350 µg/mL (INT407) and 250 µg/mL (SiHa) cell lines [62]. The present results confirm that MgO NFs are biocompatible and non-cytotoxic, consistent with previous studies, supporting their potential use in wound dressing, drug delivery, nutritional supplements, and active food packaging applications.

3.10. Toxicity assessment of MgO NFs in A. salina nauplii

The brine shrimp (Artemia salina) is an invertebrate organism widely used as a standard model for marine ecotoxicity and nanoparticle toxicity assessment. The A. salina nauplii assay provides a rapid, cost-effective, and simple method for evaluating potential toxicity. In this study, the synthesized MgO NFs were evaluated for toxicity against A. salina at the nauplii stage. The MgO NF-treated groups showed no mortality at 24 and 48 h compared with the control group. The exposure of nauplii to various concentrations of MgO NFs (0.25, 0.50, 0.75, and 1.00 mg/mL) produced no lethal effects (Figure.11). The treatment did not affect the swimming behavior or induce fatigue in the nauplii. Microscopic observations revealed the bioaccumulation of MgO NFs within the digestive tract; however, this accumulation did not cause observable toxicity.

Previous studies support these findings. Rajendran et al. reported that biosynthesized hematite nanoparticles exhibited no toxicity toward A. salina nauplii at concentrations of 0-10 mg/mL [63]. Similarly, Esakkirajan et al. (2024) demonstrated that green-synthesized MoO_3 NPs (annealed at 700 °C) showed no mortality in *A. salina* nauplii at concentrations of 0.25-1.00 mg/mL [64]. These results confirm the biocompatibility of MgO NFs and highlight their potential for safe biomedical and environmental applications.

3.11. Antibacterial activity of composite films

Antibacterial performance was quantified by calculating the percentage reduction (R%) of bacterial colonies (Table 2). The control PLA film shows no antibacterial activity and exhibits an R value of 0% against both *S. aureus* and *E. coli*. The incorporation of CRU into the PLA matrix enhances antibacterial activity and yields R values of 95.14% and 90.00%, corresponding to $\log_{10}$ reductions of 1.97 and 5.00, respectively. The addition of 1% F-MgO further improves antibacterial performance and results in near-total reduction 99.99% and 99.77% corresponding to $\log_{10}$ reductions of 1.99 and 2.35, respectively. The film containing 2% F-MgO achieves bacterial reduction 99.99% and 99.99% corresponding to $\log_{10}$ reductions of 1.99 and 1.46, respectively. The film loaded with 3% F-MgO exhibits maximum antibacterial efficacy ≥ 99 % against both pathogenic strains, indicating complete antibacterial efficacy, with corresponding $\log_{10}$ reductions of ≥ 2.00 and ≥ 2.00 for *S. aureus* and *E. coli*, respectively, reaching R values of complete reduction of both bacteria. The increase in R% with higher F-MgO content confirms the role of MgO in disrupting bacterial viability. Furthermore, bacterial counts were below the limit of detection (LOD), indicating extremely strong antibacterial activity. The composite films show slightly higher activity against *S. aureus* than *E. coli*, which results from differences in cell wall structure. The thick peptidoglycan layer of Gram-positive bacteria facilitates stronger interaction with MgO NFs. MgO NFs generate reactive oxygen

species (ROS) under light irradiation. The NFs produce electron-hole pairs, where electrons reduce dissolved oxygen to superoxide radicals ($\bullet O_2^-$) and holes oxidize water to hydroxyl radicals (•OH). These reactive species subsequently form hydrogen peroxide (H_2O_2), which induces oxidative damage to microbial cells. The results indicate that 3% F-MgO provides optimal antibacterial performance. Kim et al. (2019) reported that PLA films incorporated with positively surface-charged ZnO NPs (0-10 wt%) were evaluated for antibacterial activity using the JIS Z 2801 standard. The PLA/ZnO (3 wt.%) and PLA/ZnO (10 wt.%) composite films exhibited 100% antibacterial activity against *E. coli*. and *S. aureus*. However, improved physical properties at lower ZnO contents can be achieved by enhancing nanoparticle dispersibility within the PLA matrix [26]. Dai et al. (2022) reported that the PLA and PLA-ZnO NPs (3 wt.% based on the PLA wt.%) film was tested against *S. aureus* and *E. coli* broth culture method. As a result, a 0 -24 h interval of bacterial growth of both bacterial strains has significantly reduced the viable colonies as compared to the PLA film. However, with the growth of time, the antibacterial effect weakened slightly [25]. Teamsinsungvon et al. (2022) reported that PLA films incorporated with TiO_2 and Ti70:Si30 were evaluated for antimicrobial activity using the JIS Z 2801:2006 method. The PLA-based composite films exhibited excellent antibacterial activity against *E. coli* and *S. aureus*, demonstrating enhanced antimicrobial performance. However, *S. aureus* required longer contact time or higher catalyst concentrations to achieve a similar level of inhibition compared to *E. coli*. [65]. The present study demonstrates enhanced antibacterial activity in the PLA-CRU-2%-F-MgO film, with particularly strong inhibition against *S. aureus*. Notably, the PLA-CRU-3%-F-MgO film achieved 100% bacterial reduction in both strains. These findings highlight the potential of the developed films for antibacterial active food packaging applications.

3.12. Effect of PLA–CRU–F-MgO Active Packaging Films on the Physicochemical Quality and Antioxidant Properties of Grapes During Ambient Storage

Fresh grapes packaged with PLA, PLA–CRU, and PLA–CRU–F-MgO biodegradable active films were stored for 15 days under ambient conditions (25 ± 2 °C and 50 ± 5% RH). The effects of the films on weight loss, pH, titratable acidity, and DPPH radical scavenging activity were investigated to evaluate their ability to maintain the physicochemical quality of grapes during storage.

3.12.1. Visual Appearance of Grapes During Storage

Fresh grapes packaged with different biodegradable films exhibited noticeable differences in visual quality during the 15-day storage period (Figure S4). The grapes packaged with PLA alone showed rapid quality deterioration, characterized by severe browning, shriveling, and loss of freshness after 9 days, with pronounced dehydration and discoloration by day 15. Incorporation of curcumin (PLA–CRU) moderately delayed these changes; however, visible browning and shriveling were still observed at the end of storage. In contrast, grapes packaged with PLA–CRU–F-MgO active films maintained better visual quality throughout storage. Among all treatments, PLA–CRU–2% F-MgO exhibited the best preservation performance, retaining the natural color, firmness, and overall appearance of the grapes with minimal signs of dehydration or browning after 15 days. The PLA–CRU–3% F-MgO film also effectively preserved grape appearance but showed slightly greater color change than the 2% formulation during the later storage period. These observations indicate that the incorporation of silane-functionalized MgO NFs into the PLA–CRU matrix effectively delayed visual deterioration and extended the storage quality of fresh grapes [66].

3.12.2. Weight Loss

Weight loss increased progressively during 15 days of storage in all treatments (Figure 12A). Neat PLA exhibited the highest weight loss (≈28%), whereas PLA-CRU-3%-F-MgO showed the lowest (≈3%), followed by PLA-CRU-2%-F-MgO (≈4%). The incorporation of functionalized MgO nanoflakes significantly improved the moisture barrier by increasing the tortuous diffusion path and reducing water vapor transmission. Curcumin further enhanced film integrity, resulting in improved freshness and delayed dehydration of the packaged fruits.[27, 66–68] Similar findings have been reported for active PLA-based nanocomposite films.

3.12.3. pH

The pH gradually increased from approximately 3.42 to 3.82 during storage (Figure 12B), reflecting organic acid degradation and microbial activity. Fruits packaged with PLA-CRU-3%-F-MgO maintained the lowest pH increase, indicating better preservation than neat PLA. The combined antimicrobial activity of curcumin and MgO nanoflakes effectively delayed metabolic deterioration and microbial spoilage, thereby maintaining fruit quality throughout storage. Similar trends have been reported for antimicrobial nanocomposite food-packaging systems [27, 69].

3.12.4 Titratable Acidity

Titratable acidity decreased continuously during storage owing to the consumption of organic acids during respiration (Figure 12C). PLA showed the greatest decline, whereas PLA-CRU-2%-F-MgO retained the highest acidity after 15 days, indicating slower metabolic activity. The improved gas barrier and antimicrobial properties of MgO-containing films reduced respiration and delayed fruit senescence. These results

demonstrate that active nanocomposite films effectively preserve fruit acidity and extend storage quality [27, 68]. According to your graph, PLA-CRU-2%-F-MgO performs best for titratable acidity.

3.12.5. DPPH Radical Scavenging Activity

The DPPH radical scavenging activity decreased slightly after storage in all films (Figure 12D); however, PLA-CRU-3%-F-MgO retained the highest antioxidant activity (≈55%). The enhanced antioxidant performance is attributed to the synergistic interaction between curcumin and functionalized MgO NFs, which promotes sustained radical scavenging and reduces oxidative deterioration. The active nanocomposite films therefore provide effective antioxidant protection during fruit storage, consistent with previous reports on bioactive packaging materials [18, 66]

4. CONCLUSION

In this endeavour, MgO NFs were successfully synthesized via a hydrothermal method and systematically characterized in terms of physical and chemical properties. The MgO NFs exhibited flakes morphology and enhanced antibacterial activity against *S. aureus* and *E. coli* in a concentration-dependent manner. Toxicity evaluation using *A. salina* nauplii indicated bioaccumulation in the digestive tract without observable toxicity. *In vitro* studies showed a proliferative effect at 5 µg/mL (>135% cell viability) and no significant cytotoxicity at 50 µg/mL in RAW 264.7 cells, attributed to Mg^{2+} ion release and good biocompatibility. Furthermore, surface-functionalized MgO reduced agglomeration in the PLA-CRU matrix while enhancing crystallinity and interfacial interactions. The resulting nanocomposite films demonstrated strong antibacterial performance, achieving complete inhibition of *S. aureus* and *E. coli* (100%) in a dose-dependent manner. This find concluded that antibacterial PLA-CRU-3%-F-MgO nanocomposite film can be potentially used in medical and food packaging applications for the PLA-CRU-F-MgO

nanocomposite films effectively preserved fruit quality during 15 days of storage. Compared with neat PLA, the films significantly reduced weight loss, minimized pH changes, retained higher titratable acidity, and maintained greater DPPH radical scavenging activity. Among all formulations, PLA-CRU-2%-F-MgO and PLA-CRU-3%-F-MgO exhibited the best overall packaging performance, indicating their potential as an active biodegradable food packaging material

CTediT authorship contribution statement

Ramar Dharmaraj: Writing – review & editing, Writing – original draft, Methodology, Investigation, Formal analysis, Data curation, Validation, Conceptualization. **Arumugam Ayyakannu**: Writing – review & editing, Writing – original draft, Visualization, Validation, Supervision, Resources, Methodology, Investigation, Funding acquisition, Formal analysis, Data curation, Conceptualization.

Declaration of Competitive Interest

The authors hereby declare that they have no competing interests or financial conflicts of interest to disclose.

Ethical statement

No ethical approval is needed for this study.

Data Accessibility

The data supporting the study's findings will be made available upon request.

Funding

There is no external funding received.

Acknowledgment

The authors gratefully acknowledge the partial financial support and instrumentation facility provided by the Department of Higher Education, Government of Tamil Nadu, through the TNMulti-Gen Policy, TANSCHE, under G.O. (Ms) No. 20, Higher Education (K2) Department, Council Proceedings No. 131/B/2019, and MHRD-RUSA 2.0.

REFERENCES

1. Aghababai Beni A, Jabbari H (2022) Nanomaterials for Environmental Applications. Results in Engineering 15:100467. https://doi.org/10.1016/j.rineng.2022.100467

2. Elezz MA, Aboeleneen NM, Abd-ElMonem NM, Sorour FH (2025) A comprehensive review: Functional nanomaterials for renewable energy: Innovations, applications, and sustainable strategies. Next Materials 9:101001. https://doi.org/10.1016/j.nxmate.2025.101001

3. Haleem A, Javaid M, Singh RP, et al (2023) Applications of nanotechnology in medical field: a brief review. Global Health Journal 7:70–77. https://doi.org/10.1016/j.glohj.2023.02.008

4. Srinivasan LV, Rana SS (2024) A critical review of various synthesis methods of nanoparticles and their applications in biomedical, regenerative medicine, food packaging, and environment. Discov Appl Sci 6:371. https://doi.org/10.1007/s42452-024-06040-8

5. Vinukonda A, Bolledla N, Jadi RK, et al (2025) Synthesis of nanoparticles using advanced techniques. Next Nanotechnology 8:100169. https://doi.org/10.1016/j.nxnano.2025.100169

6. Baig N, Kammakakam I, Falath W (2021) Nanomaterials: a review of synthesis methods, properties, recent progress, and challenges. Mater Adv 2:1821–1871. https://doi.org/10.1039/D0MA00807A

7. Firmansyah SN, Dwiatmoko AA, Yunarti RT (2025) Hydrothermal synthesis of high surface area magnesium oxide (MgO) using ionic surfactant and their capacity as CO2 adsorbent. Vacuum 238:114188. https://doi.org/10.1016/j.vacuum.2025.114188

8. Rajabimashhadi Z, Naghizadeh R, Zolriasatein A, Esposito Corcione C (2023) Novel Synthesis of Nano Mg(OH)2 by Means of Hydrothermal Method with Different Surfactants. Nanomaterials 13:454. https://doi.org/10.3390/nano13030454

9. Jawad MS, Tanveer F, Ahsan RR, et al (2026) Hydrothermal synthesis of CuO Nanostructures: Morphology controlled approaches for multifunctional performance – A review. Journal of Physics and Chemistry of Solids 208:113018. https://doi.org/10.1016/j.jpcs.2025.113018

10. Han B, Wang C, Yang W, et al (2025) Hydrothermal synthesis of spherical nanoflower ZnO with highly sensitive isoprene sensing performance. Journal of Alloys and Compounds 1023:180176. https://doi.org/10.1016/j.jallcom.2025.180176

11. Morais ME, Griz JCZ, Brackmann R, et al (2026) Hydrothermal tuning of anatase-brookite TiO_2 nanostructures: Influence of synthesis parameters on surface charge, crystallite size, and photocatalytic activity. Catalysis Today 469:115753. https://doi.org/10.1016/j.cattod.2026.115753

12. Kasi G, Stalin N, Rachtanapun P, et al (2025) Effect of Calcination Temperatures on Crystallite Size, Particle Size, and Antimicrobial Activity of Synthesized MgO and Its Cytotoxicity. IJMS 26:4868. https://doi.org/10.3390/ijms26104868

13. Balla E, Daniilidis V, Karlioti G, et al (2021) Poly(lactic Acid): A Versatile Biobased Polymer for the Future with Multifunctional Properties—From Monomer Synthesis, Polymerization Techniques and Molecular Weight Increase to PLA Applications. Polymers 13:1822. https://doi.org/10.3390/polym13111822

14. Islam MS, Elahee GMF, Fang Y, et al (2025) Polylactic acid (PLA)-based multifunctional and biodegradable nanocomposites and their applications. Composites Part B: Engineering 306:112842. https://doi.org/10.1016/j.compositesb.2025.112842

15. Da Silva Pens CJ, Klug TV, Stoll L, et al (2024) Poly (lactic acid) and its improved properties by some modifications for food packaging applications: A review. Food Packaging and Shelf Life 41:101230. https://doi.org/10.1016/j.fpsl.2023.101230

16. Gutiérrez-Ruiz SC, Romero-Montero A, Hernández-Parra H, et al (2026) Curcumin Nanoformulations for Dermatological Applications: From Nutraceuticals to Nanocarriers. Food Frontiers 7:e70265. https://doi.org/10.1002/fft2.70265

17. Akshaykranth A, Jayarambabu N, Kumar A, et al (2022) Novel nanocomposite polylactic acid films with Curcumin-ZnO: structural, thermal, optical and antibacterial properties. Current Research in Green and Sustainable Chemistry 5:100332. https://doi.org/10.1016/j.crgsc.2022.100332

18. Roy S, Rhim J-W (2020) Preparation of bioactive functional poly(lactic acid)/curcumin composite film for food packaging application. International Journal of Biological Macromolecules 162:1780–1789. https://doi.org/10.1016/j.ijbiomac.2020.08.094

19. Kim D, Jang M, Seo J, et al (2013) UV-cured poly(urethane acrylate) composite films containing surface-modified tetrapod ZnO whiskers. Composites Science and Technology 75:84–92. https://doi.org/10.1016/j.compscitech.2012.12.007

20. Mousavi M, Fini E (2020) Silanization Mechanism of Silica Nanoparticles in Bitumen Using 3-Aminopropyl Triethoxysilane (APTES) and 3-Glycidyloxypropyl Trimethoxysilane (GPTMS). ACS Sustainable Chem Eng 8:3231–3240. https://doi.org/10.1021/acssuschemeng.9b06741

21. Maluin FN, Katas H (2022) Chitosan functionalization of metal- and carbon-based nanomaterials as an approach toward sustainability tomorrow. Nanotoxicology 16:425–449. https://doi.org/10.1080/17435390.2022.2090025

22. Bușilă M, Mușat V, Textor T, Mahltig B Synthesis and characterization of antimicrobial textile finishing based on Ag:ZnO nanoparticles/chitosan biocomposites

23. Farouk A, Moussa S, Ulbricht M, et al (2014) ZnO-modified hybrid polymers as an antibacterial finish for textiles. Textile Research Journal 84:40–51. https://doi.org/10.1177/0040517513485623

24. Lallo Da Silva B, Caetano BL, Chiari-Andréo BG, et al (2019) Increased antibacterial activity of ZnO nanoparticles: Influence of size and surface modification. Colloids and Surfaces B: Biointerfaces 177:440–447. https://doi.org/10.1016/j.colsurfb.2019.02.013

25. Dai L, Li R, Liang Y, et al (2022) Development of Pomegranate Peel Extract and Nano ZnO Co-Reinforced Polylactic Acid Film for Active Food Packaging. Membranes 12:1108. https://doi.org/10.3390/membranes12111108

26. Kim I, Viswanathan K, Kasi G, et al (2019) Poly(Lactic Acid)/ZnO Bionanocomposite Films with Positively Charged ZnO as Potential Antimicrobial Food Packaging Materials. Polymers 11:1427. https://doi.org/10.3390/polym11091427

27. Mukhtar A, Shah MAR, Li H, et al (2026) Multifunctional bioactive films based on carboxymethyl cellulose/sodium alginate incorporated with DES-lignin-stabilized ginger oil nanoemulsion and gallic acid for enhanced shelf-life of cherry tomatoes. Food Hydrocolloids 181:112952. https://doi.org/10.1016/j.foodhyd.2026.112952

28. Huang Z, Wu Z, Luo Z, et al (2025) Development of temperature-sensitive and controlled-release PLA-based film for strawberry preservation. Food Packaging and Shelf Life 50:101561. https://doi.org/10.1016/j.fpsl.2025.101561

29. Attri P, Sharma SR, Mittal TC, et al (2026) Comprehensive evaluation of the impact of different packaging films on the storage life and quality of tomatoes under ambient and cold storage conditions. Eur Food Res Technol 252:58. https://doi.org/10.1007/s00217-025-04967-9

30. Sagadevan S, Lett JA, Fatimah I, et al (2022) Photocatalytic and Electrochemical Activity of Magnesium Oxide Nanoballs Synthesized via a Hydrothermal Route. Processes 10:2098. https://doi.org/10.3390/pr10102098

31. Bindhu MR, Umadevi M, Kavin Micheal M, et al (2016) Structural, morphological and optical properties of MgO nanoparticles for antibacterial applications. Materials Letters 166:19–22. https://doi.org/10.1016/j.matlet.2015.12.020

32. Karthik K, Dhanuskodi S, Gobinath C, et al (2019) Fabrication of MgO nanostructures and its efficient photocatalytic, antibacterial and anticancer performance. Journal of Photochemistry and Photobiology B: Biology 190:8–20. https://doi.org/10.1016/j.jphotobiol.2018.11.001

33. Selvam NCS, Kumar RT, Kennedy LJ, Vijaya JJ (2011) Comparative study of microwave and conventional methods for the preparation and optical properties of novel MgO-micro and nano-structures. Journal of Alloys and Compounds 509:9809–9815. https://doi.org/10.1016/j.jallcom.2011.08.032

34. Zahir MdH, Rahman MM, Irshad K, Rahman MM (2019) Shape-Stabilized Phase Change Materials for Solar Energy Storage: MgO and Mg(OH)2 Mixed with Polyethylene Glycol. Nanomaterials 9:1773. https://doi.org/10.3390/nano9121773

35. Ansari A, Ali A, Asif M, Shamsuzzaman S (2018) Microwave-assisted MgO NP catalyzed one-pot multicomponent synthesis of polysubstituted steroidal pyridines. New J Chem 42:184–197. https://doi.org/10.1039/C7NJ03742B

36. Muhaymin A, Mohamed HEA, Hkiri K, et al (2024) Green synthesis of magnesium oxide nanoparticles using Hyphaene thebaica extract and their photocatalytic activities. Sci Rep 14:20135. https://doi.org/10.1038/s41598-024-71149-0

37. Nga NK, Thuy Chau NT, Viet PH (2020) Preparation and characterization of a chitosan/MgO composite for the effective removal of reactive blue 19 dye from aqueous solution. Journal of Science: Advanced Materials and Devices 5:65–72. https://doi.org/10.1016/j.jsamd.2020.01.009

38. Li C-P, Weng M-C, Huang S-L (2020) Preparation and Characterization of pH Sensitive Chitosan/3-Glycidyloxypropyl Trimethoxysilane (GPTMS) Hydrogels by Sol-Gel Method. Polymers 12:1326. https://doi.org/10.3390/polym12061326

39. Saliba PA, Mansur AA, Santos DB, Mansur HS (2015) Fusion-bonded epoxy composite coatings on chemically functionalized API steel surfaces for potential deep-water petroleum exploration. Appl Adhes Sci 3:22. https://doi.org/10.1186/s40563-015-0052-2

40. Chopra S, Pande K, Puranam P, et al (2023) Explication of mechanism governing atmospheric degradation of 3D-printed poly(lactic acid) (PLA) with different in-fill pattern and varying in-fill density. RSC Adv 13:7135–7152. https://doi.org/10.1039/D2RA07061H

41. Balamurugan S, Ashna L, Parthiban P (2014) Synthesis of Nanocrystalline MgO Particles by Combustion Followed by Annealing Method Using Hexamine as a Fuel. Journal of Nanotechnology 2014:1–6. https://doi.org/10.1155/2014/841803

42. Abbas IK, Adim KA (2023) Synthesis and characterization of magnesium oxide nanoparticles by atmospheric non-thermal plasma jet. Kuwait Journal of Science 50:223–230. https://doi.org/10.1016/j.kjs.2023.05.008

43. Jamshidian M, Tehrany EA, Imran M, et al (2010) Poly-Lactic Acid: Production, Applications, Nanocomposites, and Release Studies. Comp Rev Food Sci Food Safe 9:552–571. https://doi.org/10.1111/j.1541-4337.2010.00126.x

44. Weng Q-H, Hu M-H, Wang J-F, Hu J-J (2025) Enhancing the Flexibility and Hydrophilicity of PLA via Polymer Blends: Electrospinning vs. Solvent Casting. Polymers 17:800. https://doi.org/10.3390/polym17060800

45. Fouda A, Hassan SE-D, Saied E, Hamza MF (2021) Photocatalytic degradation of real textile and tannery effluent using biosynthesized magnesium oxide nanoparticles (MgO-NPs), heavy metal adsorption, phytotoxicity, and antimicrobial activity. Journal of Environmental Chemical Engineering 9:105346. https://doi.org/10.1016/j.jece.2021.105346

46. Ahmad A, Khan M, Khan S, et al (2023) Bio-construction of MgO nanoparticles using Texas sage plant extract for catalytical degradation of methylene blue via photocatalysis. Int J Environ Sci Technol 20:1451–1462. https://doi.org/10.1007/s13762-022-04090-2

47. Shaktawat S, Verma R, Singh KR, Singh J (2024) Biogenic-magnesium oxide nanoparticles from *Bauhinia variegata* (Kachnar) flower extract: a sustainable electrochemical approach for vitamin-B_{12} determination in real fruit juice and milk. Sustainable Food Technol 2:447–460. https://doi.org/10.1039/D3FB00198A

48. Alaizeri ZM, Alhadlaq HA, Aldawood S, et al (2021) Facile Synthesis, Characterization, Photocatalytic Activity, and Cytotoxicity of Ag-Doped MgO Nanoparticles. Nanomaterials 11:2915. https://doi.org/10.3390/nano11112915

49. Kasi G, Thanakkasaranee S, Stalin N, et al (2024) Enhancement of antimicrobial properties and cytocompatibility through silver and magnesium doping strategies on copper oxide nanocomposites. Journal of Alloys and Compounds 1007:176481. https://doi.org/10.1016/j.jallcom.2024.176481

50. Wang F, Ta N, Shen W (2014) MgO nanosheets, nanodisks, and nanofibers for the Meerwein–Ponndorf–Verley reaction. Applied Catalysis A: General 475:76–81. https://doi.org/10.1016/j.apcata.2014.01.026

51. Diru M, Lungu I, Potlog T (2025) Comparative study oF MgO nanoparticles synthesized in the presence of sodium dodecyl sulphate and aloe vera. Chem J Mold 20:33–44. https://doi.org/10.19261/cjm.2025.1344

52. Kamaraj C, Yanto DHY, Kumarasamy V, et al (2026) Magnesium Oxide Nanoparticles Loaded with 6-Gingerol: A Bioinspired Approach to Anticancer, Anti-Inflammatory, and Antioxidant Therapy. IJN Volume 21:1–22. https://doi.org/10.2147/IJN.S531933

53. Burke PJ, Bayindir Z, Kipouros GJ (2012) X-ray Photoelectron Spectroscopy (XPS) Investigation of the Surface Film on Magnesium Powders. Appl Spectrosc 66:510–518. https://doi.org/10.1366/11-06372

54. K K S, Saji A, Chanda A, Vasundhara M (2022) Effects of Calcinations Temperatures on Structural, optical and magnetic properties of MgO nanoflakes and its photocatalytic applications. Optical Materials 132:112777. https://doi.org/10.1016/j.optmat.2022.112777

55. Mondal K, Soundararajan N, Goud VV, Katiyar V (2024) Cellulose Nanocrystals Modulate Curcumin Migration in PLA-Based Active Films and Its Application as Secondary Packaging. ACS Sustainable Chem Eng 12:9642–9657. https://doi.org/10.1021/acssuschemeng.4c00518

56. Li Y, Guo C, Yang J, et al (2006) Evaluation of antioxidant properties of pomegranate peel extract in comparison with pomegranate pulp extract. Food Chemistry 96:254–260. https://doi.org/10.1016/j.foodchem.2005.02.033

57. Akshaykranth A, Jayarambabu N, Tumu VR, Rajaboina RK (2021) Comparative Study on Antibacterial Activity of MgO Nanoparticles Synthesized from Lawsonia inermis Leaves Extract and Chemical Methods. J Inorg Organomet Polym 31:2393–2400. https://doi.org/10.1007/s10904-021-01915-4

58. Periakaruppan R, Ariuthayan B, Vanathi P, et al (2025) Fabrication of Allium cepa–assisted magnesium oxide nanoparticles with antibacterial and antioxidant properties. Biomass Conv Bioref 15:22491–22498. https://doi.org/10.1007/s13399-023-04828-z

59. Thamizharasan S, Gurunathan K, Varaprasad K, Chandrasekaran K (2024) Green engineering of MgO nanoparticles: Assessment of their antioxidant and antibacterial activity against dental pathogens. Inorganic Chemistry Communications 169:113025. https://doi.org/10.1016/j.inoche.2024.113025

60. Ge S, Wang G, Shen Y, et al (2011) Cytotoxic effects of MgO nanoparticles on human umbilical vein endothelial cells *in vitro*. IET Nanobiotechnol 5:36–40. https://doi.org/10.1049/iet-nbt.2010.0022

61. Mittag A, Schneider T, Westermann M, Glei M (2019) Toxicological assessment of magnesium oxide nanoparticles in HT29 intestinal cells. Arch Toxicol 93:1491–1500. https://doi.org/10.1007/s00204-019-02451-4

62. Patel MK, Zafaryab Md, Rizvi MMA, et al (2013) Antibacterial and Cytotoxic Effect of Magnesium Oxide Nanoparticles on Bacterial and Human Cells. J Nanoengng Nanomfg 3:162–166. https://doi.org/10.1166/jnan.2013.1122

63. Rajendran K, Pujari L, Krishnamoorthy M, et al (2021) Toxicological evaluation of biosynthesised hematite nanoparticles in vivo. Colloids and Surfaces B: Biointerfaces 198:111475. https://doi.org/10.1016/j.colsurfb.2020.111475

64. Esakkirajan M, Kumaraguru S, Gopinath K, Suresh J (2024) Environmentally sustainable synthesis of MoO3 nanoparticles: Antibacterial efficacy and biocompatibility assessment. Chemical Physics Impact 8:100487. https://doi.org/10.1016/j.chphi.2024.100487

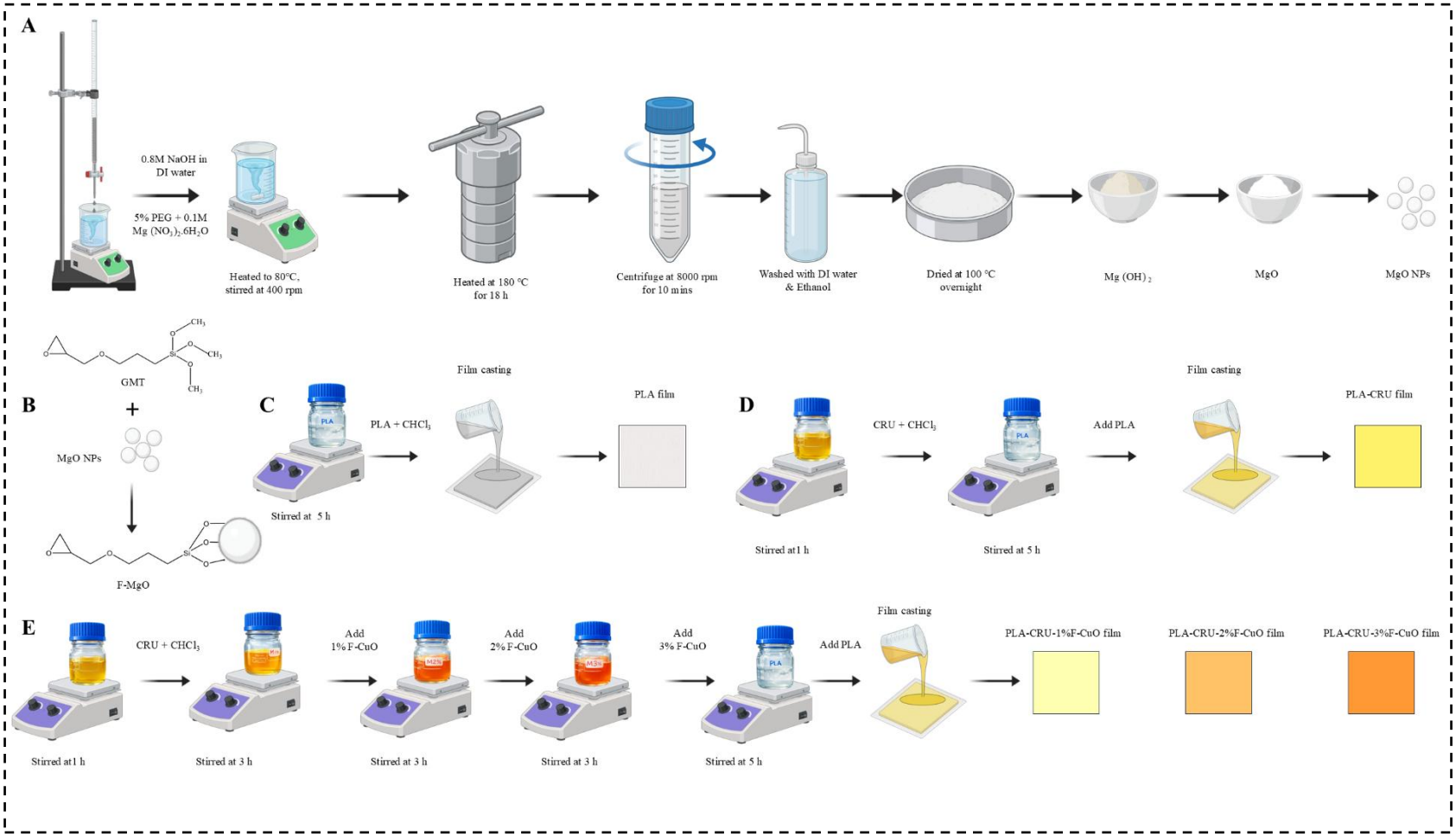
65. Teamsinsungvon A, Ruksakulpiwat C, Ruksakulpiwat Y (2022) Effects of Titanium–Silica Oxide on Degradation Behavior and Antimicrobial Activity of Poly (Lactic Acid) Composites. Polymers 14:3310. https://doi.org/10.3390/polym14163310

66. Acquavia MA, Benítez JJ, Guzmán-Puyol S, et al (2024) Enhanced extraction of bioactive compounds from tea waste for sustainable polylactide-based bioplastic applications in active food packaging. Food Packaging and Shelf Life 46:101410. https://doi.org/10.1016/j.fpsl.2024.101410

67. Siracusa V (2012) Food Packaging Permeability Behaviour: A Report. International Journal of Polymer Science 2012:1–11. https://doi.org/10.1155/2012/302029

68. Ncube LK, Ude AU, Ogunmuyiwa EN, et al (2020) Environmental Impact of Food Packaging Materials: A Review of Contemporary Development from Conventional Plastics to Polylactic Acid Based Materials. Materials 13:4994. https://doi.org/10.3390/ma13214994

69. Rhim J-W, Park H-M, Ha C-S (2013) Bio-nanocomposites for food packaging applications. Progress in Polymer Science 38:1629–1652. https://doi.org/10.1016/j.progpolymsci.2013.05.008



Schematic 1 outlines the preparation process: (A) MgO nanoflake synthesis, (B) functionalization to produce F-MgO, and (C-E) the development of PLA, PLA-CRU, and PLA-CRU-F-MgO nanocomposite films via solvent casting.

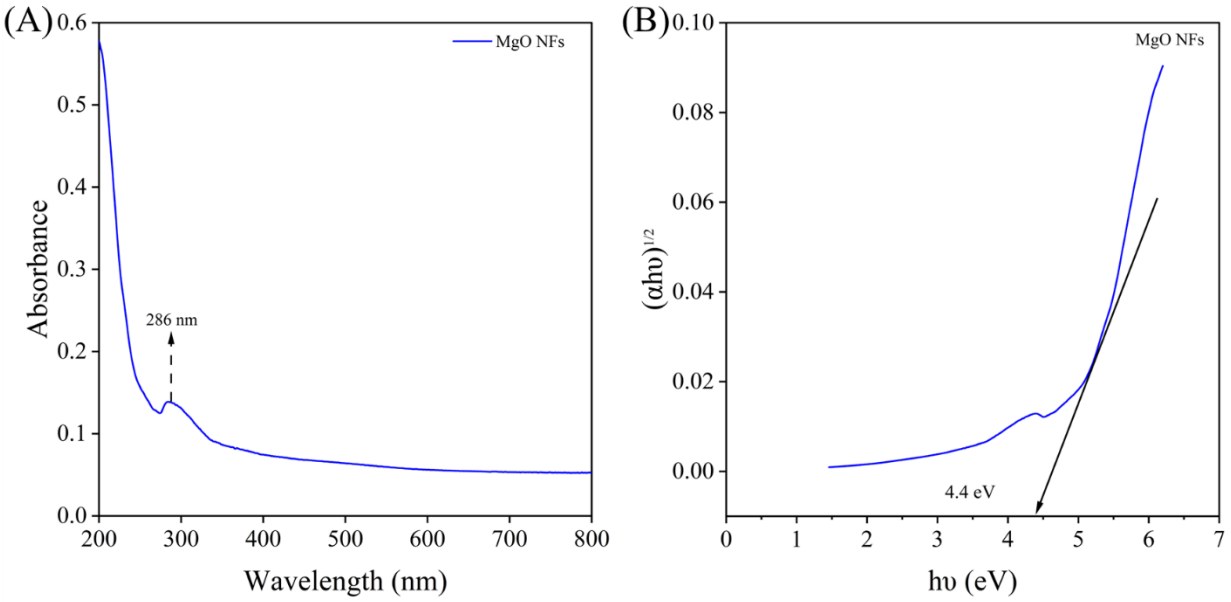


Fig. 1. (A) UV – DRS and (B) Energy Gap of synthesized MgO NFs

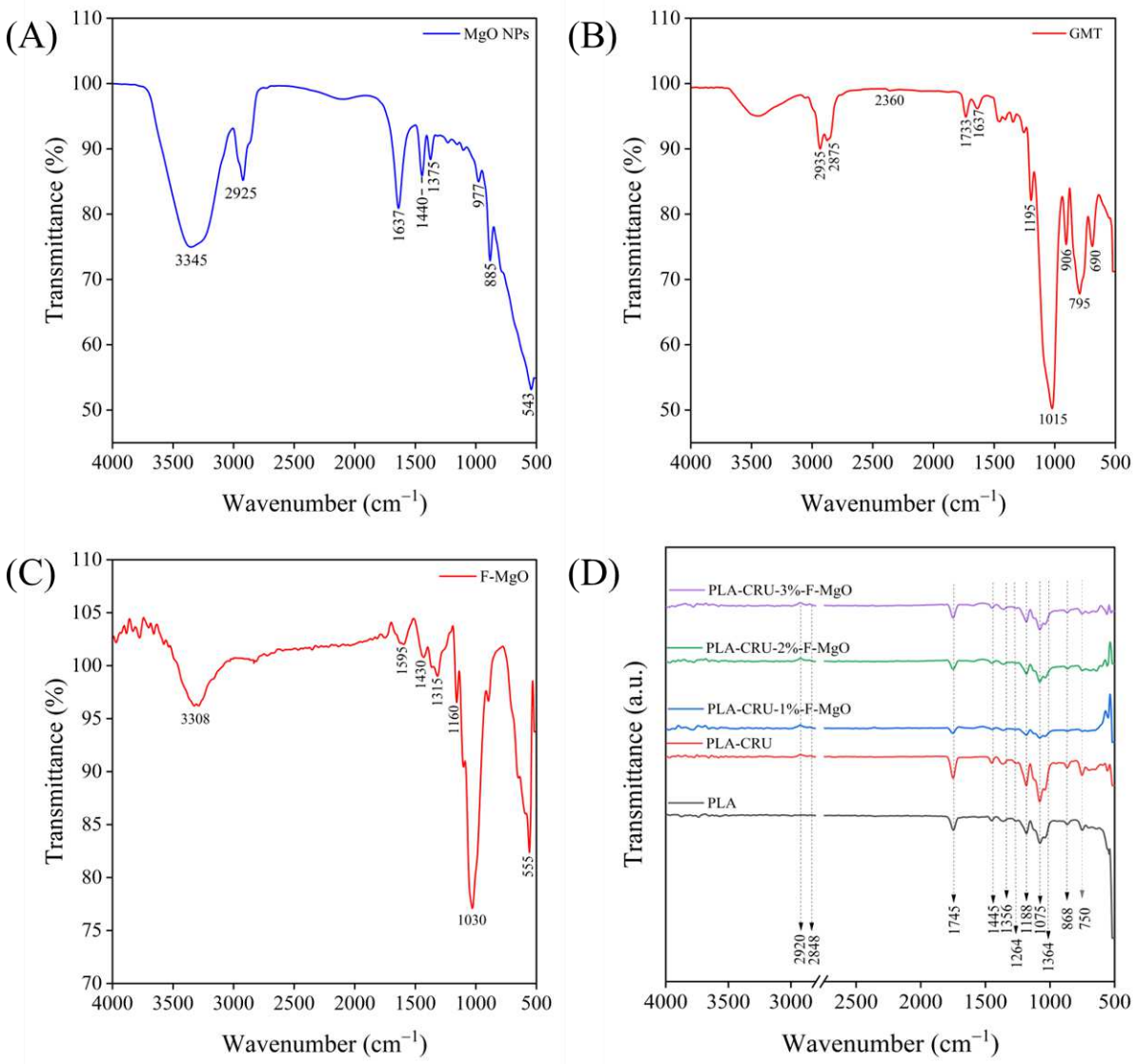


Fig.2. FTIR spectrum of (A) MgO NPs, (B) GMT, and (C) functionalized MgO NFs, along with (D) Composite film of PLA-CRU-F-MgO

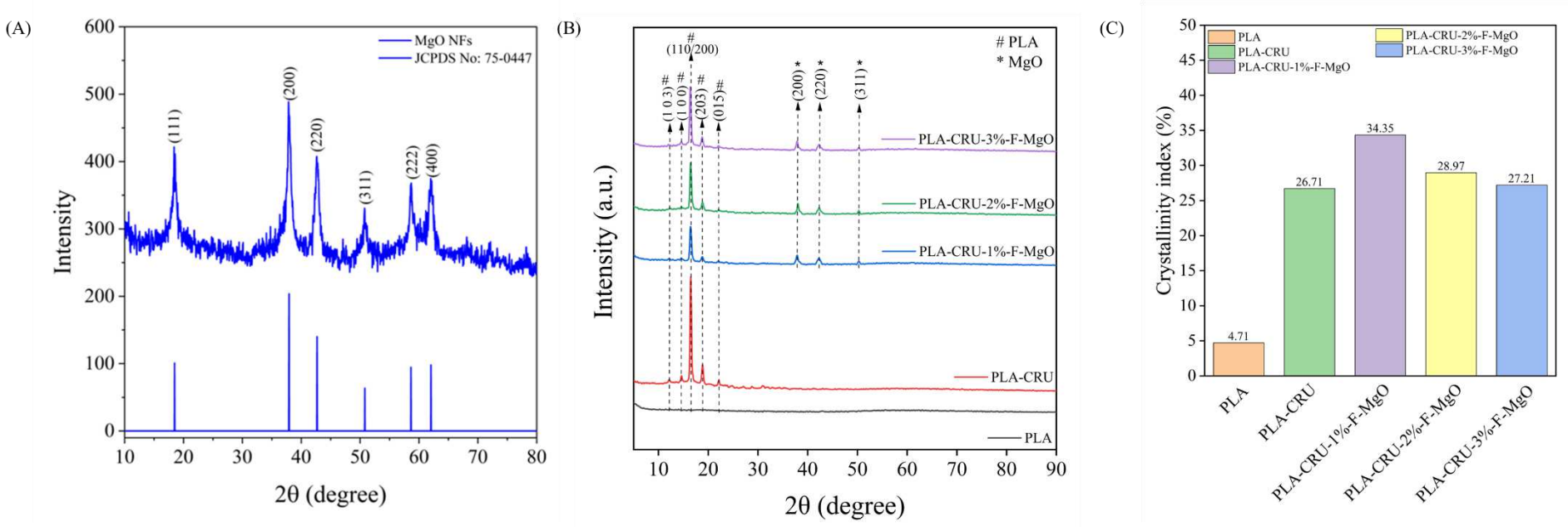


Fig. 3. (A-B) XRD patterns of MgO NFs and PLA, PLA-CUR, and PLA-CRU-F-MgO nanocomposite films and (C) crystallinity index.

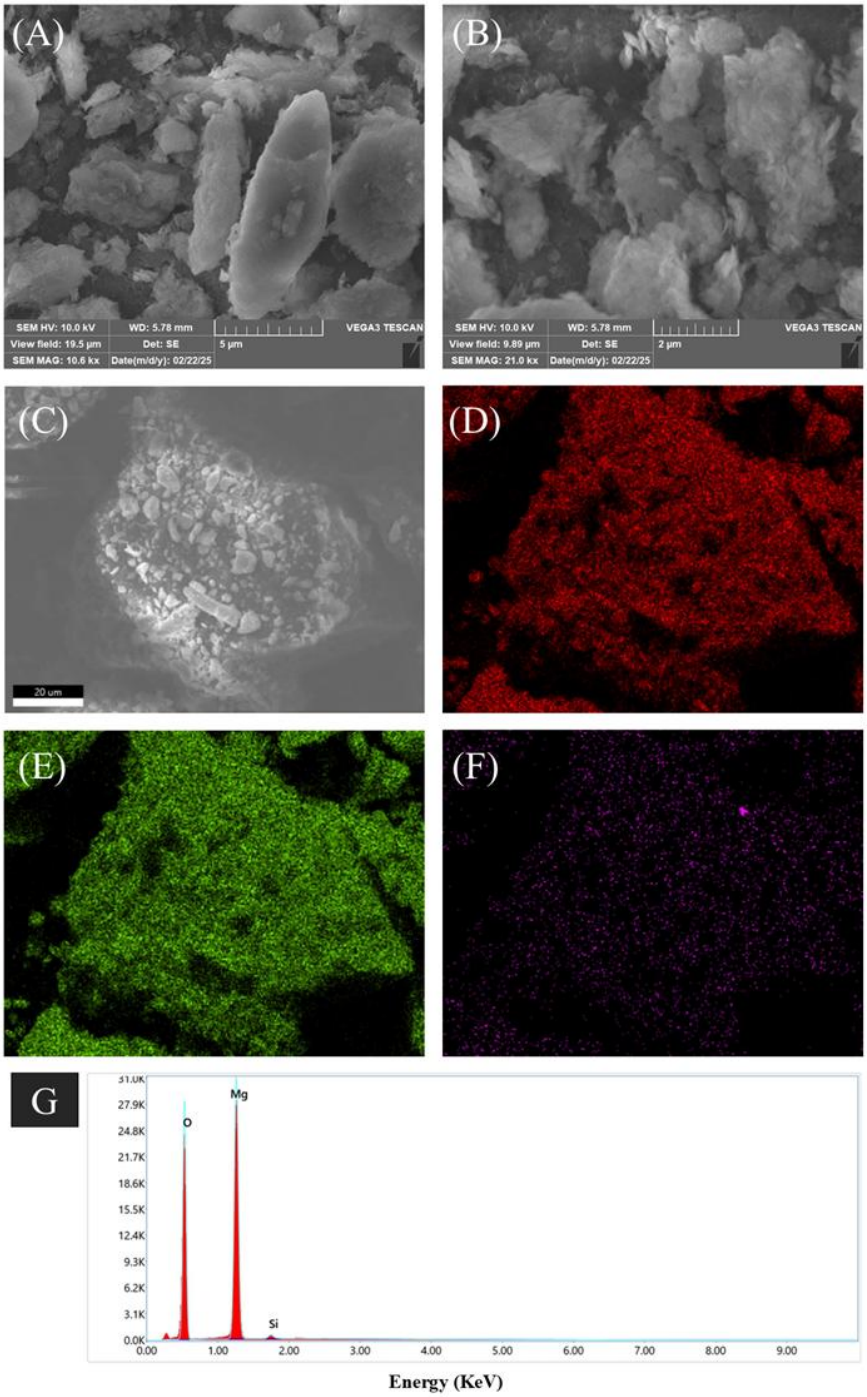


Fig. 4. (A-C) Micrographs of the synthesized MgO NFs at different magnifications, (D) elemental mapping of oxygen, (E) elemental mapping of magnesium, (F) elemental mapping of silicon, (G) EDX spectrum of MgO NFs.

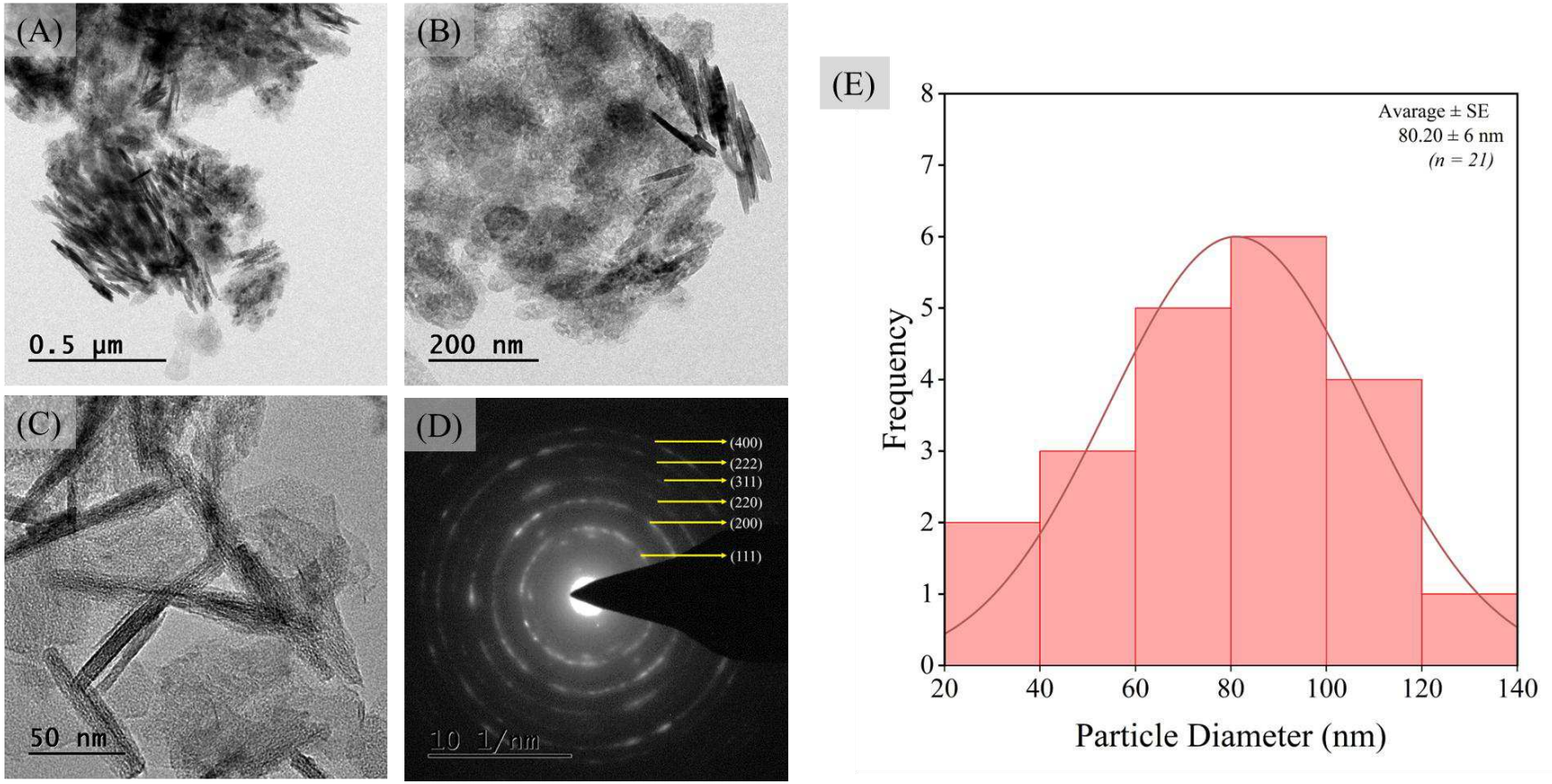


Fig. 5. (A–C) TEM images of the synthesised MgO NFs at different magnifications, (D) SAED pattern, and particle size distribution histograms of MgO NFs based on (E) Histogram of Particle Diameter.

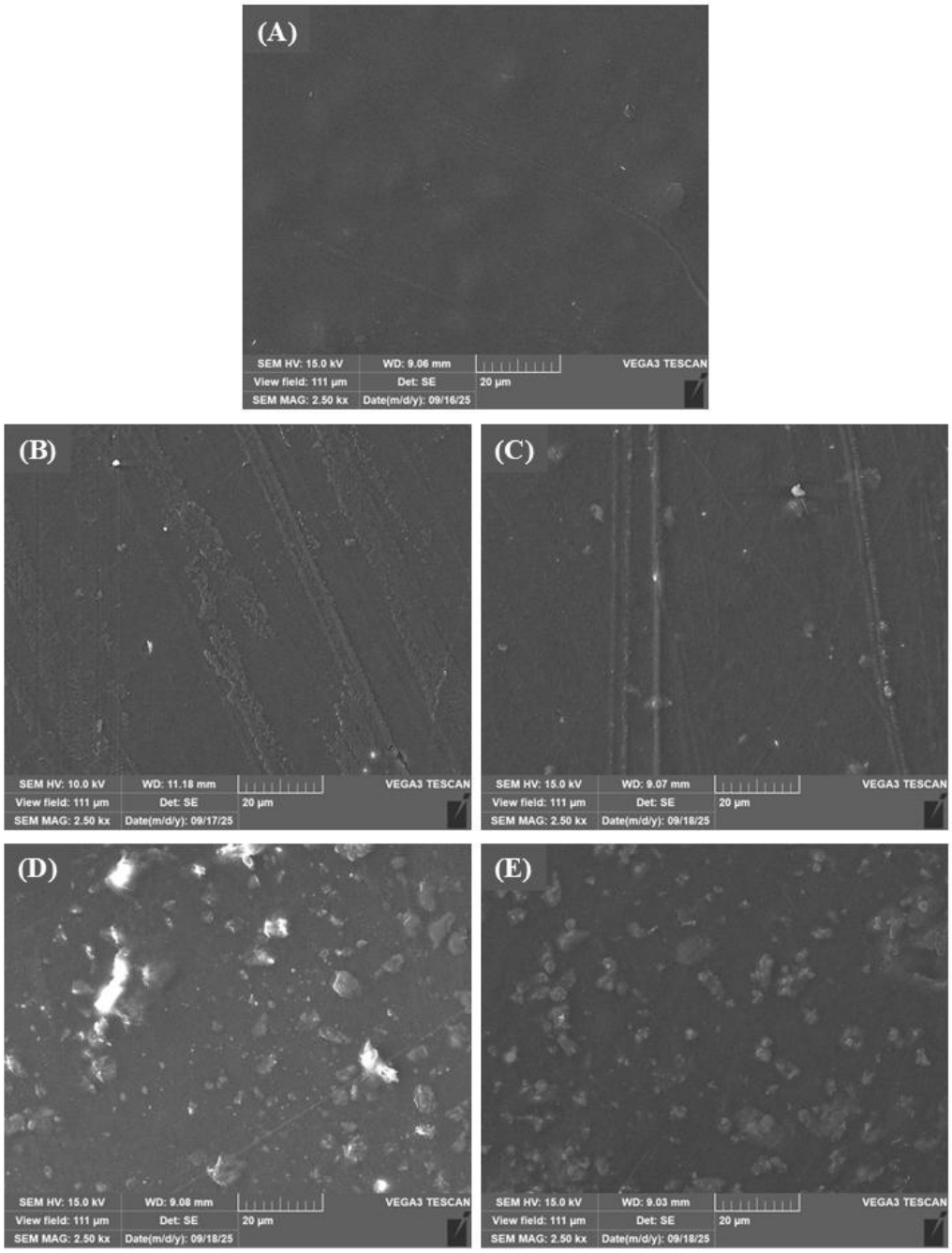


Fig. 6. Microphotographs of nanocomposite films: (A) PLA, (B) PLA-CRU, (C) PLA-CRU-1%-F-MgO, (D) PLA-CRU-2%-F-MgO, and (E) PLA-CRU-3%-F-MgO.

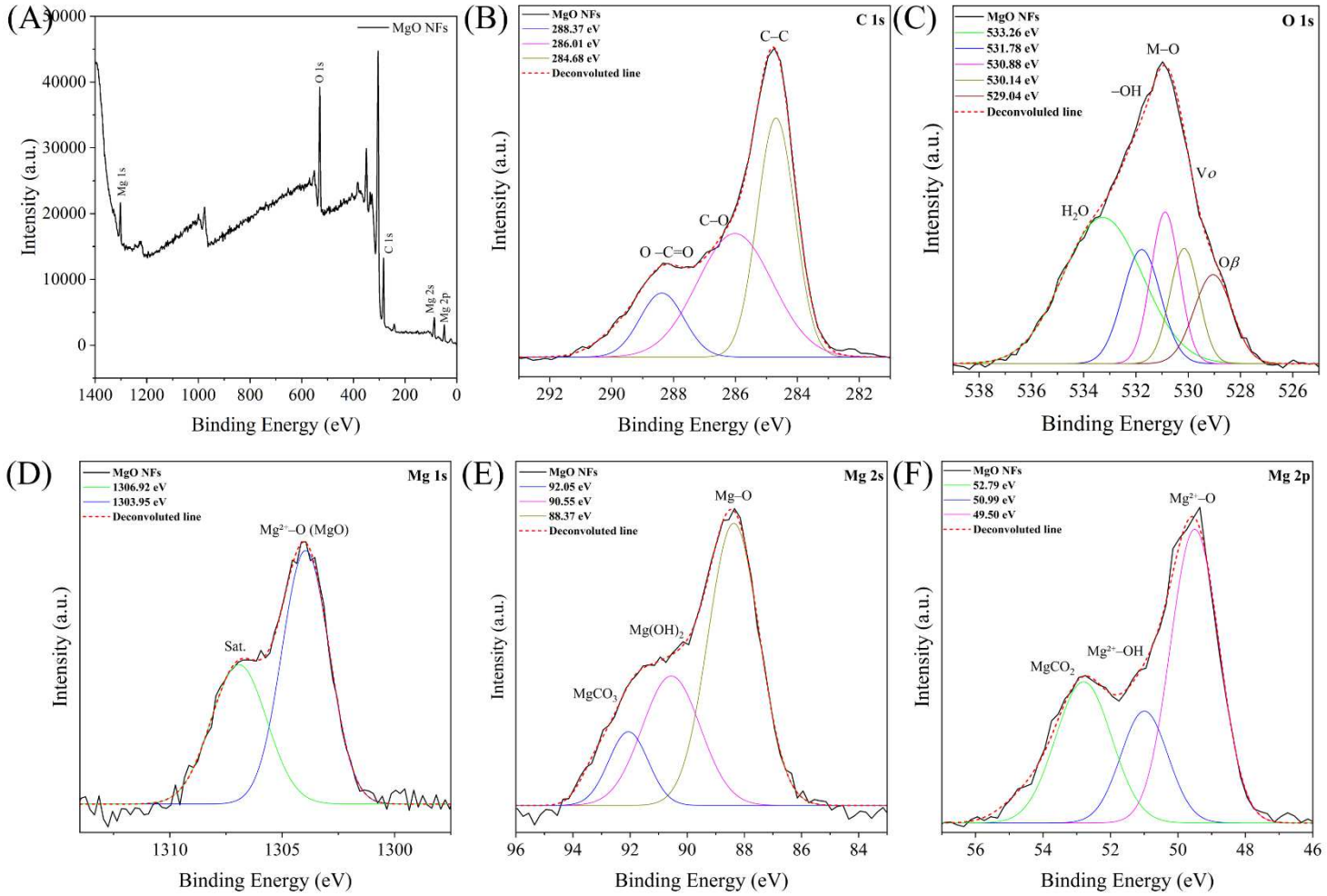


Fig. 7. X-ray photoelectron spectroscopy (XPS) analysis of MgO nanoflakes (MgO NFs): (A) survey spectrum, (B) C 1s spectrum, (C) O 1s spectrum, and (D–F) Mg core-level spectra (Mg 1s, Mg 2s, and Mg 2p).

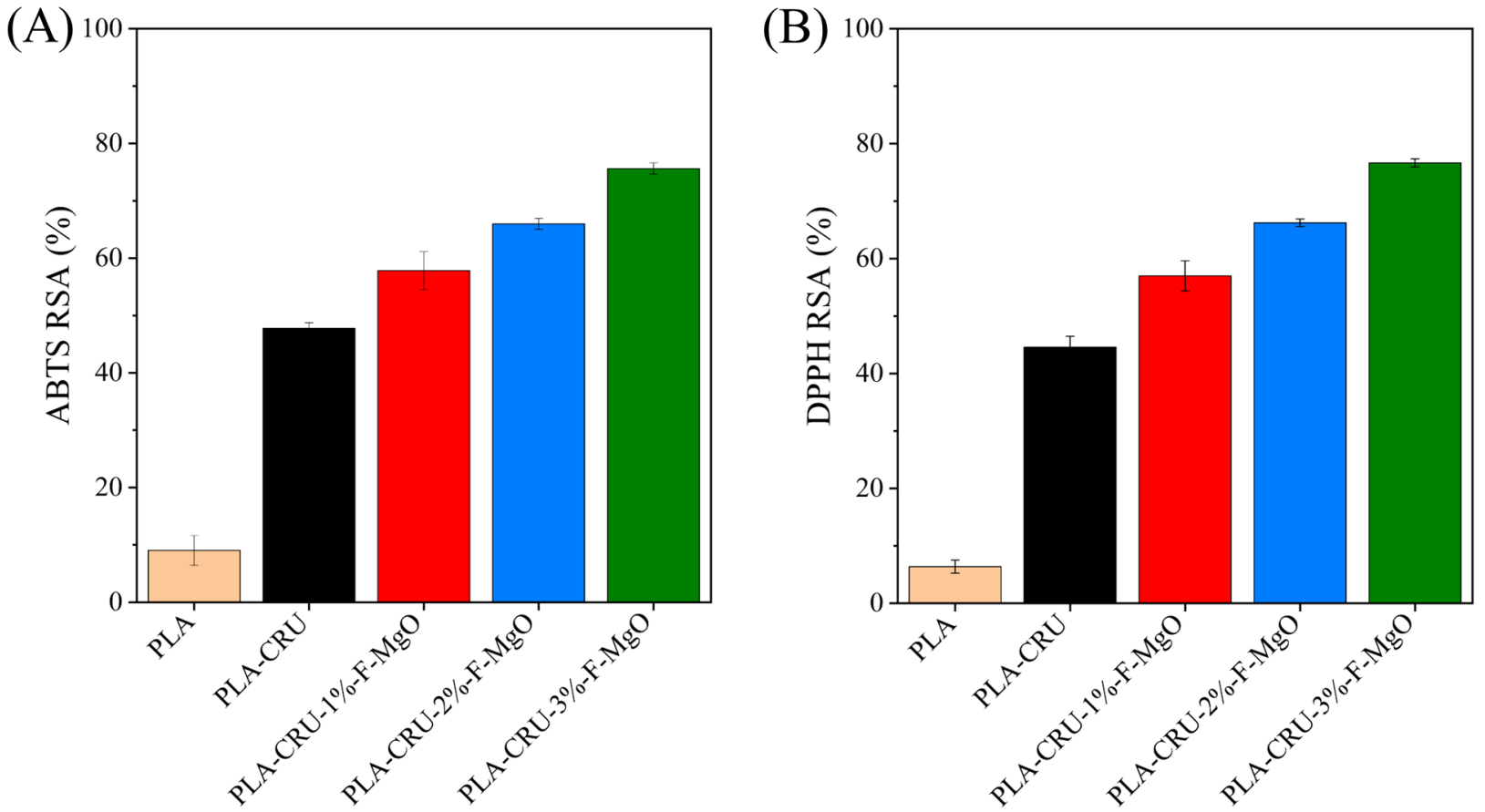


Fig. 8. Antioxidant properties of PLA–CRU-F-MgO nanocomposite films assessed by (A) ABTS and (B) DPPH radical scavenging assays.

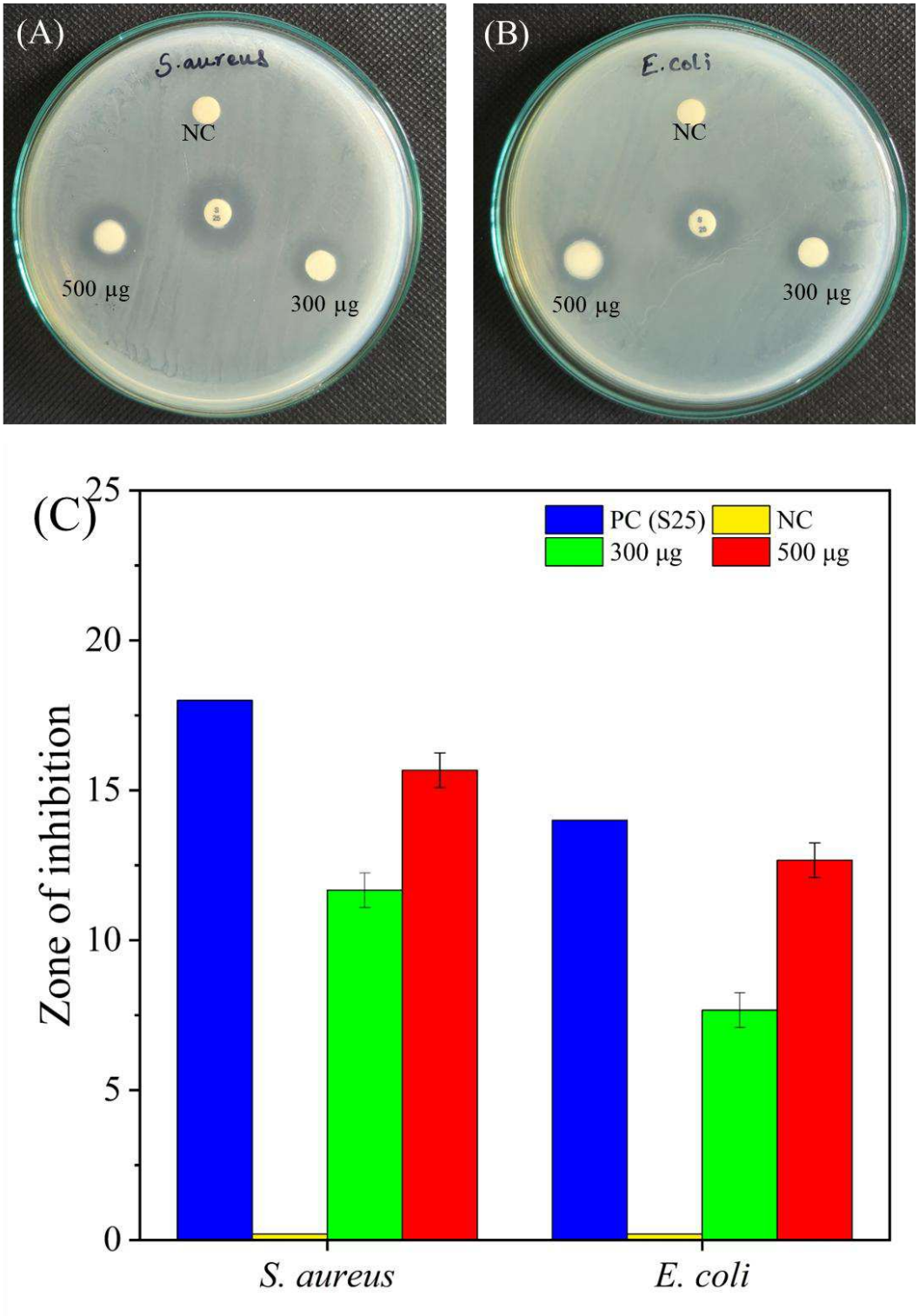


Fig. 9. Zone of inhibition of MgO NFs against (A) *Staphylococcus aureus* (Gram-positive) and (B) *Escherichia coli* (Gram-negative), and (C) optical micrograph of MgO NFs.

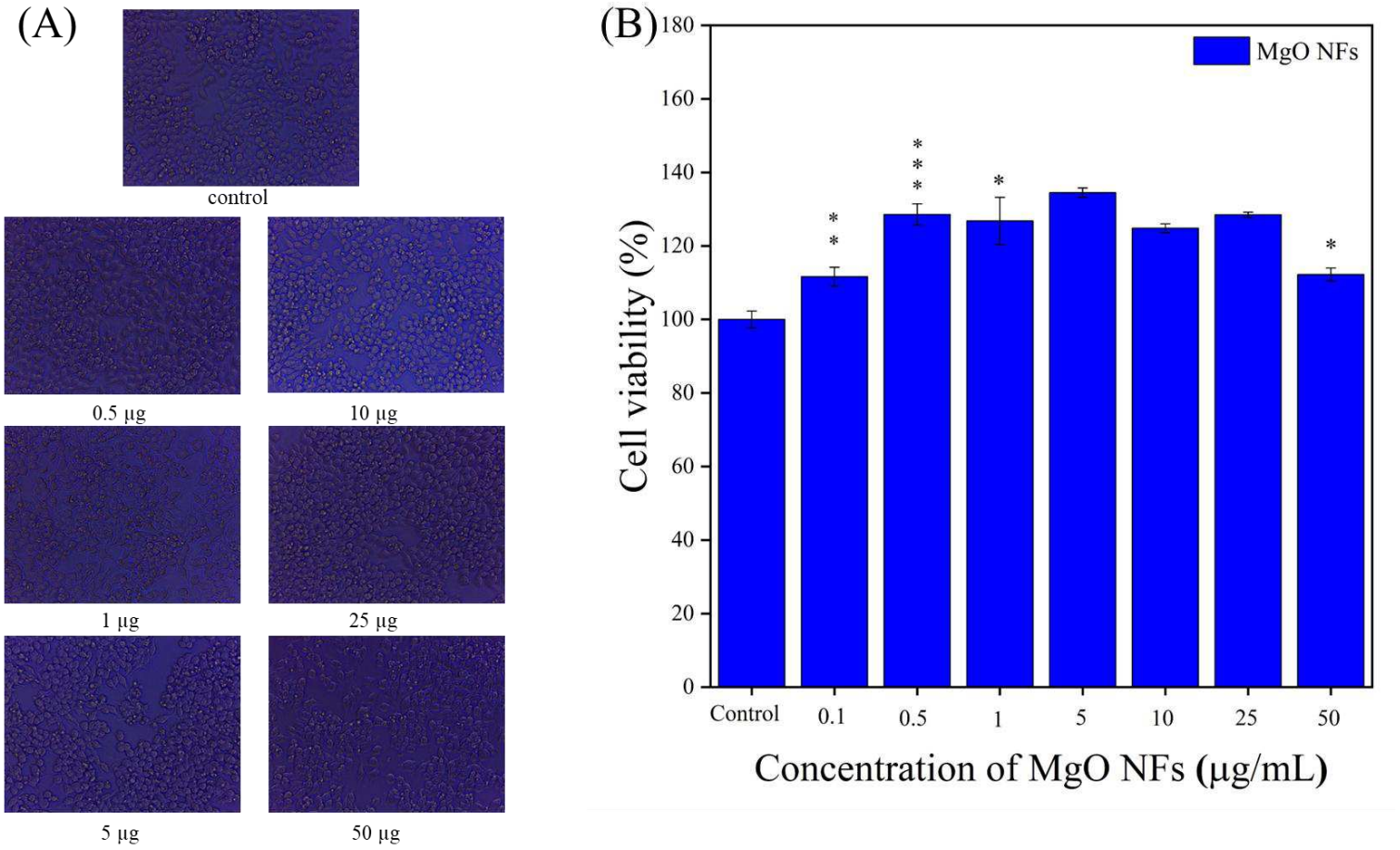


Fig 10. (A) cytotoxicity of MgO NFs at different concentrations in RAW 264.7 macrophage cells, and (B) micrographs of RAW 264.7 macrophage cells treated with MgO NFs at varying concentrations.

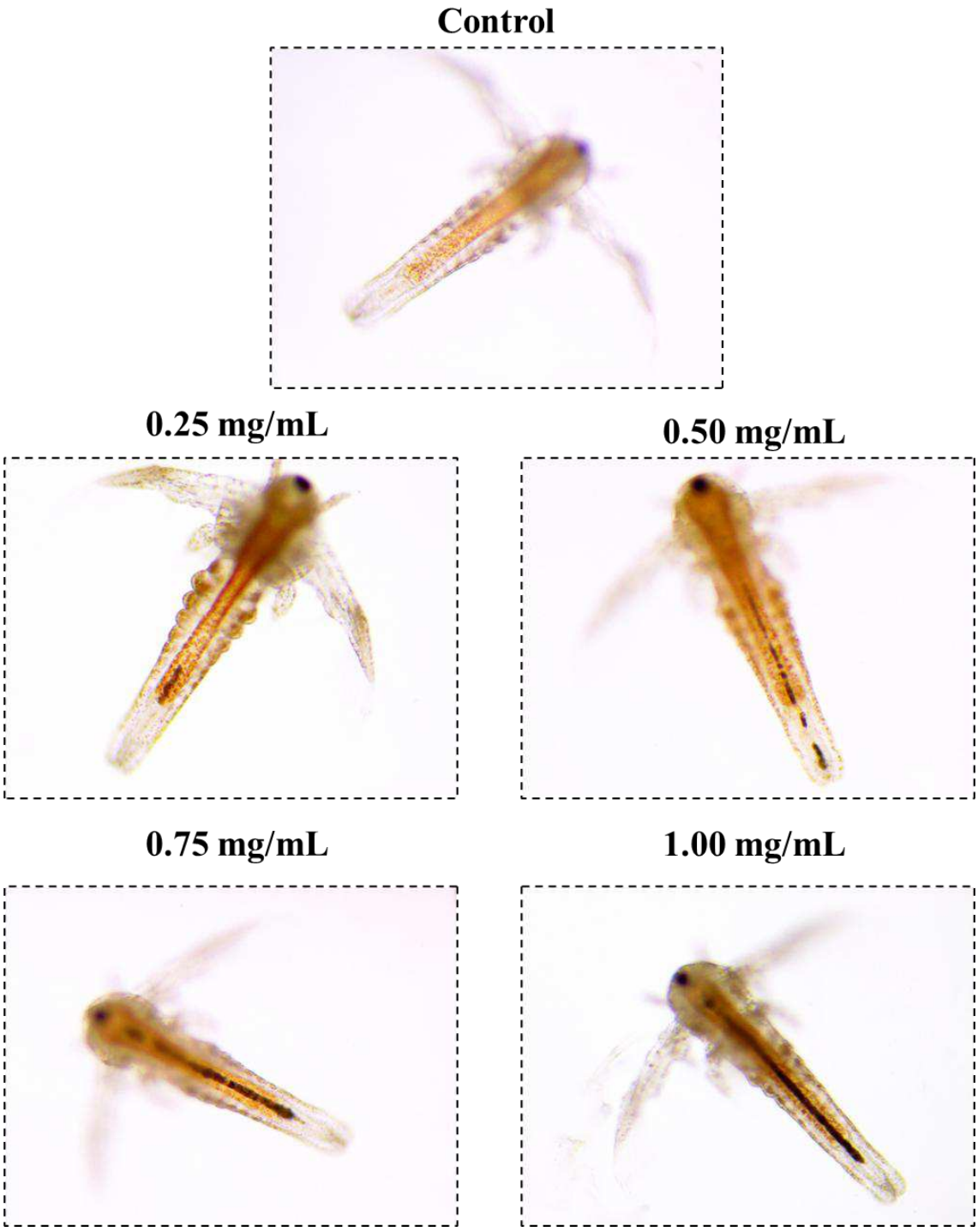


Fig 11. The MgO NFs tested against *A. salina* nauplii stage: control and different concentrations of MgO NFs (0.25, 0.50, 0.75, and 1.00 mg/ml); photos obtained at 40X resolution.

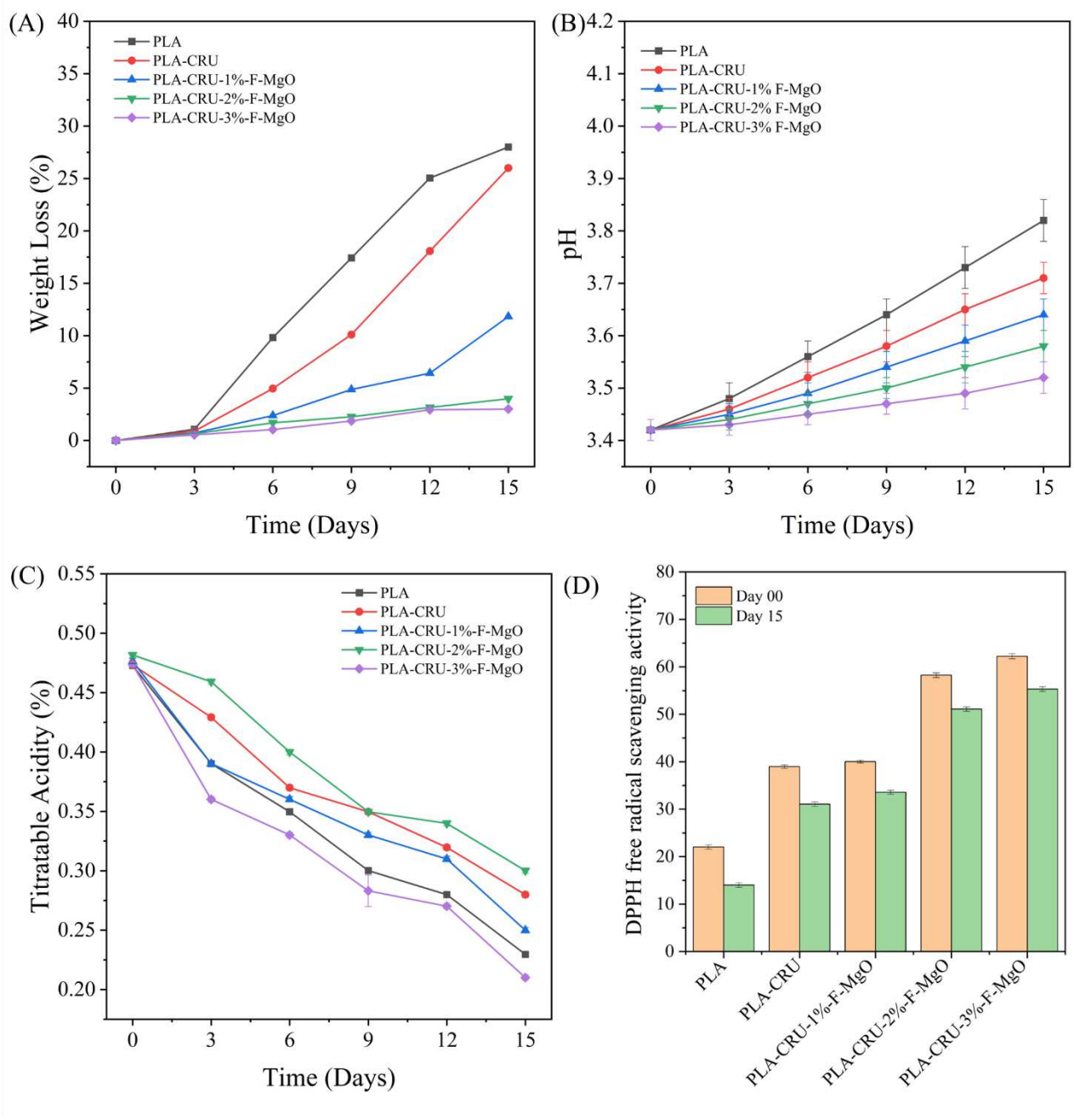


Fig 12. Physicochemical quality changes of grapes packaged with different PLA-based active films during storage at 25 ± 2 °C and 50 ± 5% RH. (A) Weight loss, (B) pH, (C) titratable acidity, and (D) DPPH radical scavenging activity.

Supplementary Files

This is a list of supplementary files associated with this preprint. Click to download.

- Tables.docx
- SupplementaryInformation.docx